CrossMark

Impacts and Statistical Mitigation of Missing Data on the 21 cm Power Spectrum: A Case Study with the Hydrogen Epoch of Reionization Array

Kai-Feng Chen[1,2,3], Michael J. Wilensky[3,4,29], Adrian Liu[3], Joshua S. Dillon[5,6], Jacqueline N. Hewitt[1,2],
Tyrone Adams[7], James E. Aguirre[8], Rushelle Baartman[7], Adam P. Beardsley[9], Lindsay M. Berkhout[3],
Gianni Bernardi[7,10,11], Tashalee S. Billings[8], Judd D. Bowman[12], Philip Bull[4,13], Jacob Burba[4], Ruby Byrne[14],
Steven Carey[15], Samir Choudhuri[16], Tyler Cox[5], David. R. DeBoer[6], Matt Dexter[6], Nico Eksteen[7], John Ely[15],
Aaron Ewall-Wice[5,6], Steven R. Furlanetto[17], Kingsley Gale-Sides[15], Hugh Garsden[4], Bharat Kumar Gehlot[12],
Adélie Gorce[18], Deepthi Gorthi[5], Ziyaad Halday[7], Bryna J. Hazelton[19,20], Jack Hickish[6], Daniel C. Jacobs[12],
Alec Josaitis[15], Nicholas S. Kern[1,2,30], Joshua Kerrigan[21], Piyanat Kittiwisit[13], Matthew Kolopanis[12],
Paul La Plante[22,23], Adam Lanman[1], Yin-Zhe Ma[24], David H. E. MacMahon[6], Lourence Malan[7], Cresshim Malgas[7],
Keith Malgas[7], Bradley Marero[7], Zachary E. Martinot[8], Lisa McBride[3,18], Andrei Mesinger[25], Nicel Mohamed-Hinds[19],
Mathakane Molewa[7], Miguel F. Morales[19], Steven G. Murray[12,25], Hans Nuwegeld[7], Aaron R. Parsons[5], Robert Pascua[3],
Yuxiang Qin[26], Eleanor Rath[1,2], Nima Razavi-Ghods[15], James Robnett[27], Mario G. Santos[7,13], Peter Sims[12],
Saurabh Singh[28], Dara Storer[19], Hilton Swarts[7], Jianrong Tan[8], Pieter van Wyngaarden[7], and Haoxuan Zheng[2]

[1] MIT Kavli Institute, Massachusetts Institute of Technology, Cambridge, MA 02139, USA; kfchen@mit.edu
[2] Department of Physics, Massachusetts Institute of Technology, Cambridge, MA 02139, USA
[3] Department of Physics and Trottier Space Institute, McGill University, Montreal QC H3A 2T8, Canada
[4] Jodrell Bank Centre for Astrophysics, University of Manchester, Manchester M13 9PL, UK
[5] Department of Astronomy, University of California, Berkeley, Berkeley, CA 94720, USA
[6] Radio Astronomy Laboratory, University of California, Berkeley, Berkeley, CA 94720, USA
[7] South African Radio Astronomy Observatory, Cape Town 7925, South Africa
[8] Department of Physics and Astronomy, University of Pennsylvania, Philadelphia, PA 19104, USA
[9] Department of Physics, Winona State University, Winona, MN 55987, USA
[10] INAF—Istituto di Radioastronomia, via Gobetti 101, 40129 Bologna, Italy
[11] Department of Physics and Electronics, Rhodes University, PO Box 94, Grahamstown 6140, South Africa
[12] School of Earth and Space Exploration, Arizona State University, Tempe, AZ 85287, USA
[13] Department of Physics and Astronomy, University of Western Cape, Cape Town 7535, South Africa
[14] Cahill Center for Astronomy and Astrophysics, California Institute of Technology, Pasadena, CA 91125, USA
[15] Cavendish Astrophysics, University of Cambridge, Cambridge CB3 0HE, UK
[16] Centre for Strings, Gravitation and Cosmology, Department of Physics, Indian Institute of Technology Madras, Chennai 600036, India
[17] Department of Physics and Astronomy, University of California, Los Angeles, CA 90095, USA
[18] Institut d'Astrophysique Spatiale, CNRS, Université Paris-Saclay, 91405 Orsay, France
[19] Department of Physics, University of Washington, Seattle, WA 98195, USA
[20] eScience Institute, University of Washington, Seattle, WA 98195, USA
[21] Department of Physics, Brown University, Providence, RI 02912, USA
[22] Department of Computer Science, University of Nevada, Las Vegas, NV 89154, USA
[23] Nevada Center for Astrophysics, University of Nevada, Las Vegas, NV 89154, USA
[24] Department of Physics, Stellenbosch University, Matieland 7602, South Africa
[25] Scuola Normale Superiore, 56126 Pisa, PI, Italy
[26] Research School of Astronomy and Astrophysics, Australian National University, Canberra, ACT 2611, Australia
[27] National Radio Astronomy Observatory, Socorro, NM 87801, USA
[28] Raman Research Institute, Sadashivanagar, Bangalore 560080, India

Abstract

The precise characterization and mitigation of systematic effects is one of the biggest roadblocks impeding the detection of the fluctuations of cosmological 21 cm signals. Missing data in radio cosmological experiments, often due to radio frequency interference (RFI), pose a particular challenge to power spectrum analysis as this could lead to the ringing of bright foreground modes in the Fourier space, heavily contaminating the cosmological signals. Here we show that the problem of missing data becomes even more arduous in the presence of systematic effects. Using a realistic numerical simulation, we demonstrate that partially flagged data combined with systematic effects can introduce significant foreground ringing. We show that such an effect can be mitigated through inpainting the missing data. We present a rigorous statistical framework that incorporates the process of inpainting missing data into a quadratic estimator of the 21 cm power spectrum. Under this framework, the uncertainties associated with our inpainting method and its impact on power spectrum statistics can be understood. These results are applied to

---

[29] CITA National Fellow.
[30] NASA Hubble Fellow.

the latest Phase II observations taken by the Hydrogen Epoch of Reionization Array, forming a crucial component in power spectrum analyses as we move toward detecting 21 cm signals in the ever more noisy RFI environment.

Unified Astronomy Thesaurus concepts: Observational cosmology (1146); Radio interferometry (1346); H I line emission (690)

1. Introduction

The redshifted 21 cm signal from neutral hydrogen contains rich astrophysical and cosmological information across cosmic time (for a review, see S. R. Furlanetto et al. 2006; J. R. Pritchard & A. Loeb 2012). Observations of such a signal will open up large volumes of the unexplored Universe, allowing us to constrain initial conditions of star and galaxy formation and to better understand the dark sector of our Universe (T.-C. Chang et al. 2008; M. F. Morales & J. S. B. Wyithe 2010; P. Bull et al. 2015; A. Mesinger 2016). In particular, radio interferometers have been built or proposed to detect the spatial fluctuation of the 21 cm signal to probe large-scale structures, the epoch of reionization (EoR), and the cosmic dawn. The high spectral resolution that can be achieved in radio astronomy makes these experiments especially advantageous for probing small-scale fluctuations along the line of sight. Examples of these experiments include the Donald C. Baker Precision Array for Probing the EoR (PAPER; A. R. Parsons et al. 2010), the LOw Frequency Array (LOFAR; M.P. van Haarlem et al. 2013), the New extension in Nançay upgrading LOFAR (NenuFAR; P. Zarka et al. 2012), the Murchison Widefield Array (MWA; S. J. Tingay et al. 2013; R. B. Wayth et al. 2018), the (upgraded) Giant Metrewave Radio Telescope (GMRT; G. Paciga et al. 2013; Y. Gupta et al. 2017), the MeerKAT telescope (M. Santos et al. 2016), the Canadian Hydrogen Intensity Mapping Experiment (CHIME; CHIME Collaboration et al. 2022), the Hydrogen Epoch of Reionization Array (HERA; D. R. DeBoer et al. 2017; L. M. Berkhout et al. 2024), the Canadian Hydrogen Observatory and Radio-transient Detector (CHORD; K. Vanderlinde et al. 2019), the Owens Valley Long Wavelength Array (OVRO-LWA; M. W. Eastwood et al. 2019), the Hydrogen Intensity and Real-time Analysis eXperiment (HIRAX; D. Crichton et al. 2022), and the Square Kilometre Array (SKA; M. Santos et al. 2015; L. Koopmans et al. 2015). While none of these experiments have reported a direct detection of the 21 cm power spectrum on its own beyond redshift $z \sim 1$ so far (S. Paul et al. 2023), many efforts have been put in to derive sensitive upper limits on the 21 cm power spectrum at various redshifts (A. Ghosh et al. 2011; G. Paciga et al. 2013; J. S. Dillon et al. 2014, 2015; A. R. Parsons et al. 2014; A. P. Beardsley et al. 2016; A. Ewall-Wice et al. 2016; A. Patil et al. 2017; N. Barry et al. 2019; M. W. Eastwood et al. 2019; B. K. Gehlot et al. 2019; M. Kolopanis et al. 2019; W. Li et al. 2019; F. G. Mertens et al. 2020; C. M. Trott et al. 2020; A. Chakraborty et al. 2021; H. Garsden et al. 2021; S. Yoshiura et al. 2021; Z. Abdurashidova et al. 2022; HERA Collaboration et al. 2023; M. J. Wilensky et al. 2023; S. Munshi et al. 2024).

The main challenge to the successful measurement of the 21 cm power spectrum lies in mitigating the bright foreground emission. Radio emission from astrophysical foregrounds can be many orders of magnitude brighter than the cosmological signals. Ideally, the spectral smoothness of the foreground emission could allow one to localize the foreground signature in the Fourier space (known as the *foreground wedge*; A. Datta et al. 2010; A. R. Parsons et al. 2012; C. M. Trott et al. 2012;

H. Vedantham et al. 2012; M. F. Morales et al. 2012; B. J. Hazelton et al. 2013; N. Thyagarajan et al. 2013; A. Liu et al. 2014), making it possible to either model and subtract the foreground, or filter and avoid the foreground (see A. Liu & J. R. Shaw 2020, for a review). Unfortunately, the lack of a perfect characterization of one's instrument could hinder these foreground mitigation strategies as any unknown spectral variations could lead to a leakage of bright foreground modes out of their intrinsically localized region. Examples of these instrumental systematic effects include calibration errors (N. Barry et al. 2016; A. H. Patil et al. 2016; A. Ewall-Wice et al. 2017; R. Byrne et al. 2019; A. Mouri Sardarabadi & L. V. E. Koopmans 2019; J. S. Dillon et al. 2020), incomplete or incorrect knowledge of the antenna response (A. R. Neben et al. 2016a; T. Ansah-Narh et al. 2018; R. C. Joseph et al. 2018; N. Orosz et al. 2019; R. C. Joseph et al. 2020; S. Choudhuri et al. 2021; H. Kim et al. 2022), or internal cable reflections, signal chain crosstalk, and mutual coupling of antennas (A. Ewall-Wice et al. 2016; N. S. Kern et al. 2019; D. C. X. Ung et al. 2020; A.T. Josaitis et al. 2022; E. Rath et al. 2024).

In addition to systematic effects arising from the instrumental signal processing chain, a growing concern for cosmological experiments in the radio band is the increasing amount of radio frequency interference (RFI). RFI from terrestrial and satellite communications can be observed even by telescopes located in extremely radio-quiet sites (J. Bowman & A. E. E. Rogers 2010; A. R. Offringa et al. 2013; A. R. Offringa et al. 2015; M. Sokolowski et al. 2016; I. Sihlangu et al. 2020; L. Lourenço et al. 2024). The impact of RFI on the 21 cm power spectrum is twofold: while most RFI is bright and can be easily identified and masked in the data (e.g., A. R. Offringa et al. 2012; M. J. Wilensky et al. 2019), residual faint RFI can still introduce power comparable to the cosmological signal across a wide range of Fourier modes (M. J. Wilensky et al. 2023); second, even if all the RFI is perfectly flagged, the gaps in data created by flagged channels are particularly problematic for power spectrum analyses as these discontinuities along the frequency axis may give rise to ringing of bright foreground modes in the Fourier space. Owing in part to the continuously deploying satellite constellations (D. Grigg et al. 2023; F. Di Vruno et al. 2023), the ever more noisy RFI environment makes mitigating the impacts of RFI an imminent task in 21 cm cosmology.

Here, we focus on dealing with gaps in the data created by flagging RFI. A conservative approach to deal with this problem is by multiplying the data with a taper function that goes to zero near the gaps (M. Kolopanis et al. 2019) or even to directly exclude an entire integration time that is affected by RFI (M. J. Wilensky et al. 2023). However, these methods will significantly limit the accessible frequency bandwidth the experiments could probe. Moreover, tapers that are dictated by the RFI gap instead of the intrinsic properties of the instrument will, in general, be suboptimal and result in reduced sensitivity. Another common strategy to reduce the impact of gaps created by RFI is to average the data across different observations that

trace the same cosmological mode. This could be averaging across different baselines through redundant baseline averaging or *uv*-plane gridding, averaging observations of the same patch of the sky from different times (Z. Abdurashidova et al. 2022), or averaging data with the same frequency separation (S. Bharadwaj et al. 2019; S. Pal et al. 2021; K. M. A. Elahi et al. 2024). This way, only channels with RFI flags that are persistent along certain axes require further treatment. In this work, however, we use a realistic simulation to show that in the presence of varying systematic effects, single-baseline delay power spectra with only partially flagged data still exhibit foreground ringing that can be seen at current state-of-the-art sensitivity levels. This is similar to what has been identified in A. R. Offringa et al. (2019) and M. J. Wilensky et al. (2022) in the context of a gridded power spectrum estimator.

Numerous other techniques have been proposed to deal with RFI gaps by extracting information from the unflagged data. A. R. Parsons & D. C. Backer (2009) adapted the CLEAN algorithm to operate in the spectral dimension (J.A. Högbom 1974; D. H. Roberts et al. 1987), proposing an iterative deconvolution method to mitigate incomplete frequency sampling. The deconvolution-based method was applied to the PAPER and HERA analyses (A. R. Parsons et al. 2014; Z. Abdurashidova et al. 2022; HERA Collaboration et al. 2023). Another camp of methods is to fit the unflagged data with a certain set of basis functions to directly perform the transformation to the Fourier space or to *inpaint* the missing frequency channels. These methods have a long history in cosmic microwave background analyses to handle missing sky coverage (A. de Oliveira-Costa & M. Tegmark 2006; P. Abrial et al. 2008; S. M. Feeney et al. 2011; J. L. Starck et al. 2013; H. F. Gruetjen et al. 2017). For instance, G. Paciga et al. (2013) adopted a Hermite basis to perform the line-of-sight transformation; C. M. Trott et al. (2016) performed a least-square spectral analysis (LSSA; P. Vaníček 1969, 1971) to fit for Fourier coefficients in MWA data; A. Patil et al. (2017), B. K. Gehlot et al. (2019), and F. G. Mertens et al. (2020) also partly utilized the LSSA method for the LOFAR data, while N. Barry et al. (2019) adopted the similar Lomb–Scargle method (N. R. Lomb 1976; J. D. Scargle 1982) for the MWA data; A. Ewall-Wice et al. (2021) proposed filtering the foreground using the discrete prolate spheroidal sequence (DPSS; D. Slepian 1978), which was later applied to the CHIME observations (M. Amiri et al. 2023; CHIME Collaboration et al. 2024); lastly, many machine-learning-based methods such as Gaussian process regression (G. B. Rybicki & W. H. Press 1992; F. G. Mertens et al. 2018; A. R. Offringa et al. 2019; N. S. Kern & A. Liu 2021) and convolutional neural networks (M. Pagano et al. 2023) have also gained growing interest in the community and have been actively applied to real data.

While most of these methods perform reasonably well on data that are not heavily flagged (A. Chakraborty et al. 2022; M. Pagano et al. 2023), an important question yet to be fully addressed is how these methods impact the statistics of the power spectrum estimator. The nontrivial correlation unavoidably introduced in the Fourier space by incomplete frequency sampling and the uncertainty in these methods itself could be increasingly important as we flag more and more data. A. Ewall-Wice et al. (2021) used an empirical covariance matrix to estimate the effect of DPSS foreground filtering on power spectrum window functions. N. S. Kern & A. Liu (2021)

investigated the effect of Gaussian process regression on power spectrum window functions under the optimal quadratic estimator framework. F. Kennedy et al. (2023) and J. Burba et al. (2024) developed a Bayesian Gibbs sampling framework to estimate uncertainties in the recovered power spectra in the presence of flags. In this work, we focus on the statistical impact on the 21 cm delay spectra introduced by the DPSS inpainting method. DPSS inpainting has been shown in M. Pagano et al. (2023) to have the smallest error in inpainting narrow RFI gaps, and its linear nature allows us to more easily examine its statistical impact. We use a Bayesian framework to derive the uncertainties associated with the inpainted data. The uncertainties and correlations introduced by data inpainting are then incorporated into a quadratic estimator framework to estimate their statistical impact on the 21 cm power spectrum. Our results also take the effects of additional analysis steps such as averaging across sidereal days, and coherent and incoherent time averages into account. These results are applied to the HERA phase II observations (L. M. Berkhout et al. 2024) to construct a set of strategies to handle missing data in the upcoming 21 cm power spectrum analysis.

This paper is organized as follows. In Section 2, we give an intuition on why nonuniform data sampling can lead to foreground ringing in the presence of systematic effects. This intuition is further verified in Section 3 using a realistic simulation. In Section 4, we introduce the DPSS inpainting method and demonstrate its impact on the statistics of the power spectrum estimator through our simulations. These results are applied to data from HERA phase II observations in Section 5. Conclusions are given in Section 6.

2. Motivation

To build intuition on how nonuniform data sampling can affect the 21 cm power spectrum, consider the interferometric response of two antennas, i.e., the *visibility*, measured at a frequency ν,

$$V(\boldsymbol{b}_{ij}, \nu) = \int d\Omega \, I(\hat{s}, \nu) B_{ij}(\hat{s}, \nu) \exp\left(-\frac{i2\pi\nu}{c}\boldsymbol{b}_{ij} \cdot \hat{s}\right). \quad (1)$$

Here, i and j are antenna indices, I is the specific intensity of the sky, B_{ij} is the cross power beam, $\boldsymbol{b}_{ij}$ is the baseline vector, and $\hat{s}$ is the unit vector on the sky over which we integrate. A rough estimator of the 21cm power spectrum can then be formed as

$$\hat{P}_{21\,\text{cm},\alpha} \propto \tilde{V}^*(\boldsymbol{b}_1, \tau_\alpha) \tilde{V}(\boldsymbol{b}_2, \tau_\alpha), \quad (2)$$

where $\tilde{V}$ is obtained by taking the *delay transform* (A. R. Parsons & D. C. Backer 2009) of the visibility

$$\tilde{V}(\boldsymbol{b}, \tau) = \int d\nu \, V(\boldsymbol{b}, \nu)\gamma(\nu)\exp(-i2\pi\nu\tau), \quad (3)$$

in which $\gamma(\nu)$ is a tapering function chosen by the analyst. Throughout this work, if not otherwise specified, we choose $\gamma(\nu)$ to be the four-term Blackman–Harris window (F. J. Harris 1978; M. Kolopanis et al. 2019). In general, we can decompose the delay-transformed visibility into

$$\tilde{V} = \tilde{s} + \tilde{e} + \tilde{n}, \quad (4)$$

where s is the signal from foreground emission, e is the desired EoR signal, and n is the thermal noise. Because the foreground emission is spectrally smooth, we expect the foreground signal to be below the noise level beyond a certain delay depending

on the baseline length (A. R. Parsons et al. 2012). This creates a range in the delay space that allows us to more easily search for the EoR signal, known as the *EoR window* (A. Datta et al. 2010; A. Liu et al. 2014).

If the observation is affected by RFI, causing some of the frequency channels to be flagged, the EoR window can be contaminated. We can write the flagged visibility as $V_{\text{flagged}}(\nu) = V(\nu) \times w(\nu)$, where w is a sampling function that takes the value of 1 or 0. If we then take the delay transform of the flagged visibility, by the convolution theorem, we obtain

$$\tilde{V}_{\text{flagged}}(\tau) = (\tilde{V} \circledast \tilde{w})(\tau), \qquad (5)$$

where we use $\circledast$ to denote the convolution of two functions. As the sampling function w is a sum of multiple top hat functions, its delay transform will be of the form

$$\tilde{w}(\tau) = \sum_i a_i \text{sinc}(\pi a_i \tau) e^{i2\pi\nu_i\tau}, \qquad (6)$$

where ν_i and a_i denote the location and width of the flag, respectively. Since $\tilde{w}(\tau)$ has unbounded support, this will cause the foreground $\tilde{s}_{\text{flagged}} = \tilde{s} \circledast \tilde{w}$ to be no longer limited within a certain delay range, leading to contamination of the EoR window. This impact of missing data on power spectra is well understood in the literature in different contexts. In this work, however, we are focusing on a more subtle effect that arises from averaging over data that might contain flags.

Consider the example of a drift-scan telescope. As the earth rotates, a drift-scan 21 cm experiment can observe repeatedly at the same local sidereal time (LST) to increase sensitivity. The LST-averaged visibility after a long observation period can be written as

$$V_{\text{avg}}(\boldsymbol{b}, \nu) = \frac{\sum_i V_i(\boldsymbol{b}, \nu) \times w_i(\nu)}{\sum_i w_i(\nu)}, \qquad (7)$$

where i runs over the different sidereal days the visibility is observed on. Here, we will consider the regime where none of the frequency channels are flagged every day, i.e., $\sum_i w_i(\nu) > 0$ for all ν. In this regime, if the visibility consists only of foreground sky emission, cosmological signal, and thermal noise, the nonuniform sampling of data will have little impact on the final power spectrum since

$$V_{\text{avg}} = \frac{\sum_i (s + e + n_i) \times w_i}{\sum_i w_i}$$
$$= s + e + \frac{\sum_i n_i w_i}{\sum_i w_i}$$
$$\Rightarrow \tilde{V}_{\text{avg}} = \tilde{s} + \tilde{e} + \sum_i \tilde{K}_i \circledast \tilde{n}_i, \qquad (8)$$

where $K_i \equiv (w_i/\sum_j w_j)$ and its delay-transformed counterpart $\tilde{K}_i$ are a sum of sinc-like functions. Here, we assume only the thermal noise component n_i is different from night to night.[31] In this case, we see that the kernel $\tilde{K}_i$ induced by the nonuniform sampling only introduces correlation in the noise spectrum. Since the $\tilde{K}_i \circledast \tilde{n}_i$ terms still have zero mean, $\tilde{V}_{\text{avg}}$ is still able to

---

[31] We note that we also assume that the observation is taken at the exact same grid of LST every night. This could cease to be true in practice due to misaligned discretization in the instrument or choices made by the analysts. The presence of such a slight deviation in nightly observing time can introduce extra correlation in the power spectrum as investigated in M. J. Wilensky et al. (2022).

give us an unbiased estimate of the cosmological signal in the EoR window.

In reality, however, every component in the visibility can vary from night to night due to systematic effects. For example, gain uncertainties after calibration, small motions in the instrument, or internal instrument couplings can all introduce tiny night-to-night variations on the measured visibilities. If we quantify these nightly varying systematic effects by a multiplicative bias $(1 + \varepsilon_i)$, the resulting LST-averaged visibility would be

$$V_{\text{avg}} = \frac{\sum_i (1 + \varepsilon_i)(s + e + n_i) \times w_i}{\sum_i w_i}$$
$$= s + e + \frac{\sum_i \varepsilon_i w_i}{\sum_i w_i}(s + e) + \frac{\sum_i (1 + \varepsilon_i) n_i w_i}{\sum_i w_i}$$
$$= s + e + \sum_i \varepsilon_i K_i (s + e) + \sum_i K_i (1 + \varepsilon_i) n_i. \qquad (9)$$

Here, even if we assume the multiplicative biases ε do not depend on frequency, we see that

$$\tilde{V}_{\text{avg}} = \tilde{s} + \tilde{e} + \sum_i \varepsilon_i \tilde{K}_i \circledast (\tilde{s} + \tilde{e}) + \sum_i (1 + \varepsilon_i) \tilde{K}_i \circledast \tilde{n}_i. \qquad (10)$$

In particular, the terms proportional to $\tilde{K}_i \circledast \tilde{s}$ would lead to contamination of the EoR window due to the convolution of the kernel with the bright foreground component. We stress that such a contamination exists even though for every frequency channel we have measured some amount of good data. Moreover, unlike thermal noise, the fluctuation in the systematic effects ε_i may not be centered around zero and are usually highly uncertain, making it difficult to remove the contamination simply via averaging the data across some other axes. Quantifying and mitigating this interplay between systematic effects and nonuniform data sampling is precisely the subject of this work.

3. Simulation

As an illustration, we construct a simple interferometric array similar to HERA and simulate its response to foreground sky emission with various instrumental systematic effects. We construct a seven-element interferometric array with the antennas located on the vertices and the center of a hexagon with a side of 14.6 m. The array layout can be seen in the leftmost panel of Figure 1. Starting from Equation (1), we simulate the visibility response from point sources in the GLEAM catalog (N. Hurley-Walker et al. 2017, 2019) and the diffuse emission given by the Global Sky Model (A. de Oliveira-Costa et al. 2008; H. Zheng et al. 2017). We assume each antenna has an Airy beam profile

$$B(\hat{\mathbf{s}}(\theta, \phi); \nu) = \left[\frac{2J_1(2\pi\nu a \sin\theta/c)}{2\pi\nu a \sin\theta/c} \right]^2, \qquad (11)$$

where J_1 is the Bessel function of the first kind, θ is the zenith angle, and a is the aperture radius, which we set to be 6 m (A. R. Neben et al. 2016b; D. R. DeBoer et al. 2017). Here, we simulate the array to observe the sky every 10 s over an overlapping 1.5 hr period across 16 nights. The visibility is sampled in 120 kHz wide frequency channels to imitate the response of a HERA-like digital back end (L. M. Berkhout et al. 2024). To simulate potential night-to-night fluctuations due to systematic effects and investigate their interplay with RFI flags, we consider the following additional ingredients to our simulation:
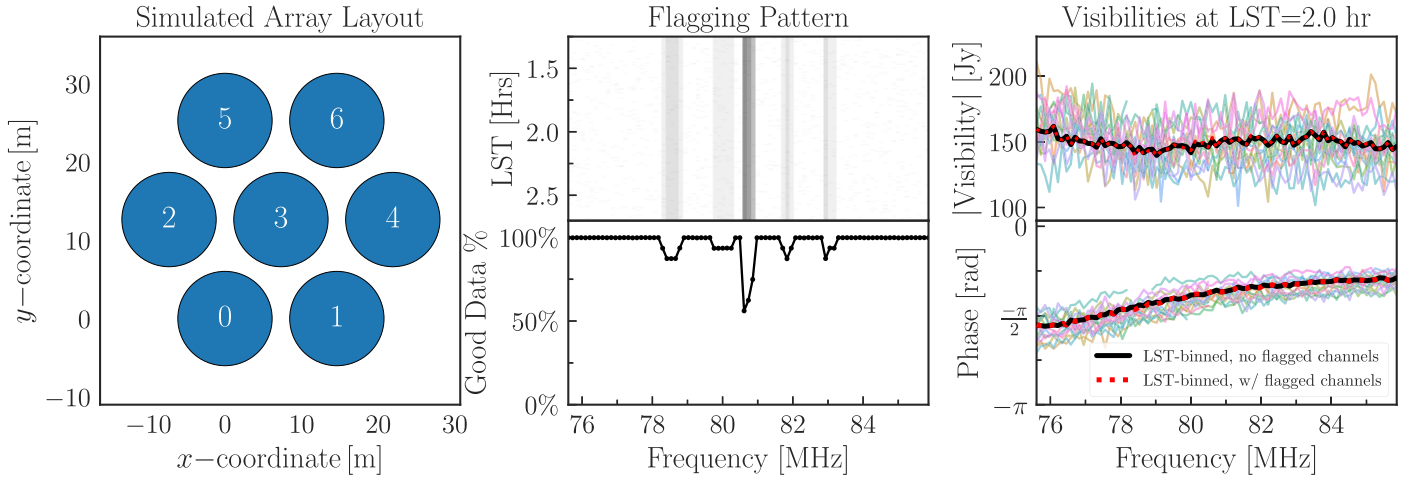
Figure 1. Left: example interferometric array layout we simulate in this work. Antennas are placed on the vertices and the center of a hexagon with a side of 14.6 m. Center: example of the simulated flagging patterns we draw in this work. The top panel shows the flagging patterns for the baseline formed by antenna 0 and 1 summed over all nights of observation. A darker color indicates a higher amount of flags. The lower panel shows the overall percentage of good data as a function of the frequency. Right: absolute value of the nightly visibilities at a particular local sidereal time (color lines) and the sidereal-day-averaged visibility with (solid black) or without (dotted black) flags.

1. *Antenna gain uncertainties.* Calibrating the instrument and solving for the antenna's gain solutions is a vital task in 21 cm cosmology. While many calibration strategies exist in the literature (D.A. Mitchell et al. 2009; S. Yatawatta et al. 2008; A. Liu et al. 2010; I. S. Sullivan et al. 2012; J. L. Sievers 2017; W. Li et al. 2018; U. Armel Mbou Sob et al. 2019; J. S. Dillon et al. 2020; P. H. Sims et al. 2022; R. Byrne 2023; T. A. Cox et al. 2024), no calibration method is perfect. Here, we consider a small uncertainty in the observed visibility V^{obs} compared to the underlying true visibility V^{true} by setting

$$V_{ij}^{\mathrm{obs}} = g_i g_j^* V_{ij}^{\mathrm{true}}, \qquad (12)$$

where i and j are antenna indices and g_j is the antenna-based complex gain uncertainty. We model $g_j \equiv 1 + (a + bi)$ with a and b randomly drawn from a uniform distribution between -0.05 and 0.05 for each antenna at each night to simulate a ~5% uncertainty in gain solutions.

2. *Beam perturbations.* Accurate descriptions of the antenna primary beam response are another key to a precise measurement of the 21 cm power spectrum. However, the antenna response can be subject to small changes due to perturbations to the instrument itself. Here, we consider another systematic effect that arises from random motions in the feed. This is modeled with a generalized antenna primary power beam profile (N. Orosz et al. 2019)

$$B_i(\hat{\mathbf{s}}(\theta, \phi); \nu) = \left[\frac{2J_1(2\pi\nu a \sin\theta'/c)}{2\pi\nu a \sin\theta'/c} \right]^2, \qquad (13)$$

where the perturbed pointing θ' is defined as

$$\sin\theta'(\theta, \phi, x_i, y_i) \equiv$$
$$\sqrt{\left(\sin\theta\cos\phi - \frac{x_i}{z}\right)^2 + \left(\sin\theta\sin\phi - \frac{y_i}{z}\right)^2}, \qquad (14)$$

in which x_i, y_i represent a small perturbation in the feed position and z is the height of the feed. Here, we assume

$z = 4.5$ m and draw x_i and y_i from a Gaussian distribution with zero mean and $\sigma = 2$ cm (E. Rath et al. 2021) for each antenna on each night of observation. The cross power beam in Equation (1) is then obtained as $B_{ij} = \sqrt{B_i B_j}$.

3. *Instrument coupling.* Another known concern for radio interferometers is the potential coupling among antennas. These couplings can occur internally in the analog signal chain due to impedance mismatches or in the field through reflections from one antenna to another. Because of the delay in signal propagation, these instrument couplings will cause the foreground signal to leak into higher delay ranges. Here, we adopt a model presented in A.T. Josaitis et al. (2022) and E. Rath et al. (2024) to simulate this effect. The coupled visibility V_{ij}^{cpl} is modeled as

$$V_{ij}^{\mathrm{cpl}} = V_{ij}^{\mathrm{true}} - \sum_{k \neq i} \Gamma \frac{V_{kj}^{\mathrm{true}}}{|\mathbf{b}_{ik}|/\lambda} e^{+i2\pi\nu|\mathbf{b}_{ik}|/c}$$
$$+ \sum_{k \neq j} \Gamma^* \frac{V_{ik}^{\mathrm{true}}}{|\mathbf{b}_{kj}|/\lambda} e^{-i2\pi\nu|\mathbf{b}_{kj}|/c}, \qquad (15)$$

where the coupling coefficient $\Gamma \equiv a + bi$ is drawn nightly by randomly choosing $a, b \in [-0.01, 0.01]$

4. *Thermal noise.* After modeling the signal and the systematic effects, we add a noise realization to each baseline for each time integration and frequency channel according to the radiometer equation and the autocorrelation visibilities (J. Tan et al. 2021)

$$\sigma_{ij}^{\mathrm{rms}}(\nu, t) = \sqrt{\frac{V_{ii}(\nu, t) V_{jj}(\nu, t)}{\Delta\nu\Delta t}}. \qquad (16)$$

Here $\sigma_{ij}^{\mathrm{rms}}$ denotes the standard deviation of the thermal noise for the visibility measured by baseline $\mathbf{b}_{ij}$, V_{ii} is the autocorrelation visibility measured by antenna i, $\Delta\nu$ is the correlator channel width, and Δt is the correlator integration time.

5. *RFI flags.* We create two types of flags for each of the antennas in our simulation during each night of

Figure 2. Comparison of power spectra of simulated flagged and unflagged visibilities from a single 14.6 m east–west baseline with various systematics effects. For a consistent comparison, we use simulated data with the exact same noise realization and the same realization for all the systematic effects. The only difference between the same line in the left and the right panel is in whether some channels are flagged or not during the sidereal-day average. The flagging pattern that goes into this particular case can be seen in Figure 1.
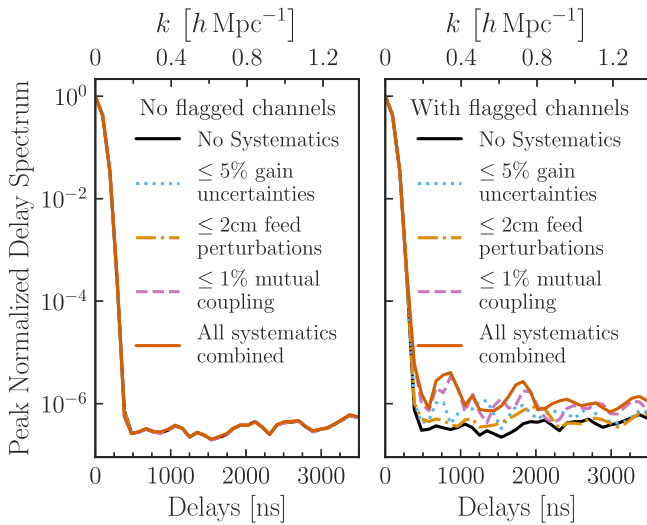
observations. First, a channel at a given time and frequency is randomly flagged according to a binomial distribution with a probability of 0.001. These flags mimic the effect from irregular short-timescale RFI sources such as airplane reflections. Second, we create RFI flags for a few frequency channels across an entire night. For each night, we identify $n \in \{0, 1, 2\}$ frequency channels that are common to all antennas to flag. We start by picking the flagged frequency channels with a uniform weighting, and the channels that have been flagged the night before will be more likely to be flagged to simulate periodic RFI sources such as satellite communications or TV stations. For each antenna, the RFI flags are centered at these frequency channels with a randomly chosen width of zero (not flagged) to three channels (the central frequency channel and the two neighboring channels are all flagged) to simulate leakage of bright RFI sources.

The middle panel of Figure 1 shows an example of the flagging patterns for one baseline in our simulation. The nightly variation in the visibilities due to changing systematic effects is shown in the rightmost panel of Figure 1. The colored lines in the top panel are nightly visibilities at a particular local sidereal time and the black lines indicate the averaged visibility with (solid) or without (dotted) flags. Although there exists only a very small difference between the two averaged visibilities, we will soon see that this could still introduce a nonnegligible effect on the power spectrum, highlighting the necessity of looking beyond frequency–time waterfall plots in diagnosing systematic effects.

Figure 2 shows the delay spectra for a single 14.6 m baseline following Equation (2). These delay spectra are formed by first coherently averaging 300 s of visibilities after phasing them to a common pointing center. The delay spectra within the 1.5 hr window of observations are then averaged incoherently to further increase the sensitivity. In Figure 2, the different color lines show the delay spectrum from the visibility with different systematics considered. These systematic effects themselves do

not have any significant impact on the power spectrum, as can be seen in the left panel of Figure 2. However, once we include flags during the sidereal-day averaging, this introduces discontinuities in the visibility which raise the noise floor by almost an order of magnitude. More quantitatively, going back to Equations (9) and (10), this demonstrates that even if we are in a regime where the systematic effect is below the noise level in the EoR window ($\bar{\varepsilon}\tilde{s} \ll \tilde{n}$ at high delays), the ringing of bright foreground modes due to RFI flags can cause these systematic effects to be more prominent.

The flagging pattern that goes into the right panel of Figure 2 is given in Figure 1. While in this example, one of the channels is flagged around half of the time, causing a more significant discontinuity in the averaged visibility, foreground ringing can occur even when only a tiny fraction of the data are flagged. Figure 3 shows the level of foreground ringing under a variety of scenarios. In all these cases, we only change the flagging patterns as shown in each of the panels on the left-hand side. For a consistent comparison, the noise realization and the systematic effects are kept the same. The bottom panel of Figure 3 shows an example in which a tiny fraction ($\lesssim 10\%$) of flagged data across the frequency range is still enough to cause contamination to the EoR window. Figure 3 also shows that the significance of this effect depends on both the width of the flags and the location of the flags. In the second panel from the top, we move the large gap from the first panel at around 80 MHz to the edge of the band, the leakage of bright foreground modes to the EoR window is significantly reduced due to the tapering function we applied. Similar effects can be seen in the third panel where we replace the wide gap in the first panel with a gap that is only a single channel wide. While carefully choosing a frequency band to estimate the power spectrum can help reduce the leakage of bright foreground modes, a mitigation strategy for these gaps in the data is required if we are to probe 21 cm power spectra at arbitrary redshifts of interest.

4. Data Inpainting

The power spectra derived from our simulation in Section 2 show us that even with channels that are flagged less than 10% of the time, one cannot simply average the remaining good data in the presence of nightly varying systematic effects. Certain mitigation strategies are still needed to avoid the low-level ringing of bright foreground modes. A common method to deal with missing data due to RFI is to fill in the data based on our best guess of the signal, known as data inpainting (A. R. Parsons & D. C. Backer 2009; G. Paciga et al. 2013; N. Barry et al. 2019; C. M. Trott et al. 2016; A. Ewall-Wice et al. 2021). Here, we will focus on a particular linear data inpainting method utilizing the DPSS (D. Slepian 1978; A. Ewall-Wice et al. 2021). Our inpainting procedure is discussed in Section 4.1. In Section 4.2 we calculate the uncertainties and correlations in the visibility introduced by the inpainting procedure. The impact of inpainting on the final power spectrum estimator is discussed in Section 4.3.

4.1. Inpainting Method

As the contamination on the EoR window comes from the ringing of bright foreground modes, in order to mitigate this effect, we would like to fill the gap in our data with our best guess of the signals from the foreground combined with systematic effects without introducing extra structures in the high-delay modes. This can be achieved by choosing a set of
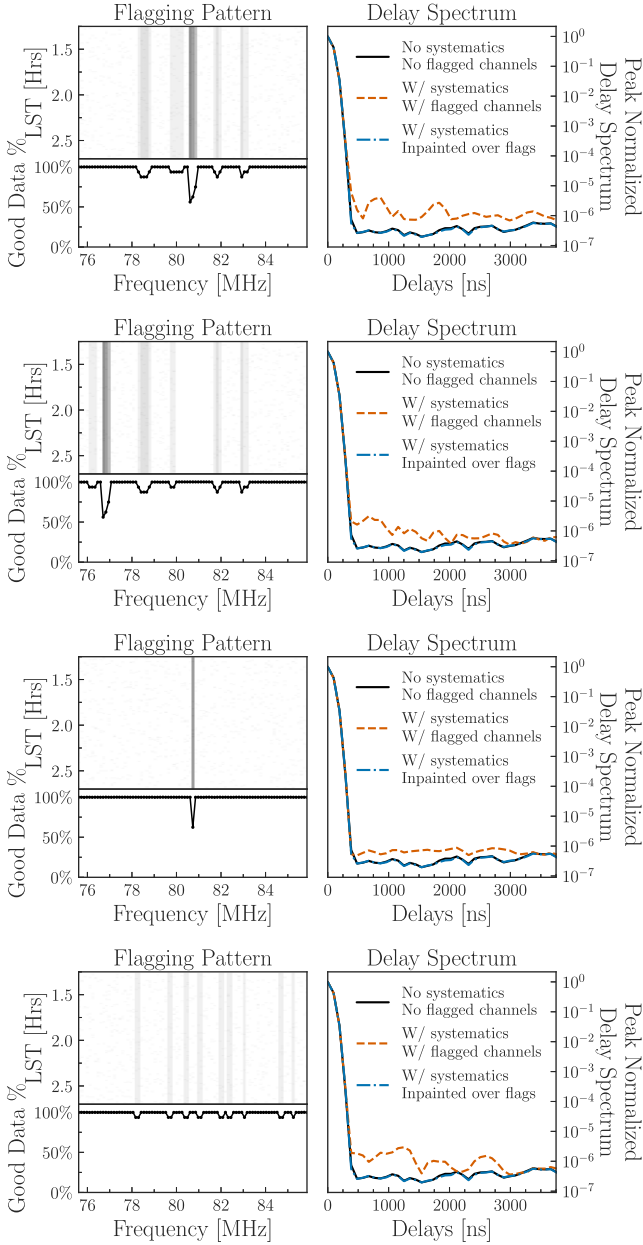
Figure 3. Power spectra with or without data inpainting under different simulated flagging patterns. Similar to Figures 1 and 2, each row shows the flagging patterns (left) and the corresponding power spectra (right) for one 14.6 m east–west baseline integrated over 16 nights. For a consistent comparison, the noise realization and the systematic effects are the same across the four different columns, the only difference is in the flagging patterns.

band-limited basis functions $f_i(\nu)$ in the frequency space with Fourier dual that is localized in a certain delay range. Such a set of basis functions is known as the discrete prolate spheroidal sequence (DPSS). Here, we follow D. Slepian (1978) and re-derive the properties of DPSS for the reader's convenience. Let $[\nu_0 - W/2, \nu_0 + W/2]$ be the frequency range where one is inpainting data, and $[-T, T]$ be the delay range we want our model to be localized in. We would like to find a sequence $f_i(\nu)$ that maximizes

$$\lambda_i \equiv \frac{\int_{-T}^{+T} |\tilde{f}_i(\tau)|^2 \, d\tau}{\int_{-\infty}^{+\infty} |\tilde{f}_i(\tau)|^2 \, d\tau}, \qquad (17)$$

where we use $\tilde{f}_i$ to denote the Fourier dual of f_i. Using the Parseval–Plancherel identity, the denominator of Equation (17) can be written as

$$\int_{-\infty}^{+\infty} |\tilde{f}_i(\tau)|^2 \, d\tau = \int_{-\infty}^{+\infty} |f_i(\nu)|^2 \, d\nu$$
$$= \int_{\nu_0 - W/2}^{\nu_0 + W/2} f_i^*(\nu) f_i(\nu) \, d\nu, \qquad (18)$$

in which we use the fact that f is band-limited. Meanwhile, the numerator of Equation (17) gives

$$\int_{-T}^{+T} |\tilde{f}_i(\tau)|^2 \, d\tau = \int_{-\infty}^{+\infty} \tilde{f}_i^*(\tau) \tilde{B}(\tau; T) \tilde{f}_i(\tau) \, d\tau$$
$$= \int_{-\infty}^{+\infty} \tilde{f}_i^*(\tau) \widetilde{B \circledast f_i}(\tau) \, d\tau$$
$$= \int_{-\infty}^{+\infty} f_i^*(\nu) (B \circledast f_i)(\nu) \, d\nu, \qquad (19)$$

where $\tilde{B}(\tau; T)$ is a top hat function in the delay space with a width of $2T$ and B is the inverse Fourier transform in the frequency space

$$B = \frac{\sin 2\pi T \nu}{\pi \nu}. \qquad (20)$$

In particular, this shows us that a set of solutions to Equation (17) can be found by solving for the band-limited eigenfunctions f_i of

$$\int_{\nu_0 - W/2}^{\nu_0 + W/2} \frac{\sin 2\pi T (\nu - \nu')}{\pi (\nu - \nu')} f_i(\nu') \, d\nu' = \lambda_i f_i(\nu). \qquad (21)$$

In the discretized version, our desired basis can be obtained by solving for the eigenvectors to the matrix

$$B_{ij} = \frac{\sin 2\pi T (\nu_i - \nu_j)}{\pi (\nu_i - \nu_j)}, \qquad (22)$$

known as the prolate matrix. The eigenvectors to the prolate matrix are precisely the DPSS. While these eigenvectors form a complete set of bases, depending on their eigenvalue, not all of them have a highly concentrated power in our desired delay range. Following Equation (17), the eigenvalues λ_i are strictly between 0 and 1. It has been shown that the eigenvalues are either close to 1 or to 0 with only a few in the transition zone (S. Karnik et al. 2020). In this work, we choose $T = 500$ ns and select f_i with $\lambda_i \geqslant 10^{-12}$ to form a set of basis functions to fit for the foreground signal in the flagged channels. A lower eigenvalue cut here ensures that we have a more complete basis for the signal that is localized in the $[-T, +T]$ delay range. While this also gives us some eigenvectors with some structure in the high-delay EoR window, the number of these eigenvectors is fairly limited. We note that ideally, the value T should be chosen at the horizon scale $\tau_H \equiv |\boldsymbol{b}|/c$ for each baseline $\boldsymbol{b}$. This allows the chosen DPSS basis to capture all the bright foreground modes without affecting the EoR window. For the shortest 14.6 m baseline in our array, $\tau_H \sim 50$ ns. In reality, one often chooses a T that is slightly larger than τ_H to also capture any foreground leakage beyond the wedge due to systematic effects. In this work, we choose $T = 500$ ns as it has been shown in data obtained by the Phase II HERA

observations that foreground can leak to such a delay due to mutual coupling of antennas (E. Rath et al. 2024).

Once a set of basis $\{f_i\}_{i=1}^N$ is chosen, we can obtain our best guess of the foreground structure parameterized by these basis functions through the unflagged data. This is achieved by finding a set of coefficients $\boldsymbol{b}$ that solves the linear system

$$\boldsymbol{v}_{\rm obs} = \boldsymbol{W}(\boldsymbol{A}\boldsymbol{b} + \boldsymbol{n}), \qquad (23)$$

where $\boldsymbol{v}_{\rm obs}$ is the observed data, $A_{ij} = f_j(\nu_i)$ is the *design matrix*, and $\boldsymbol{W}$ is a diagonal matrix that is 1 for unflagged channels and 0 otherwise. The maximum likelihood estimator of $\boldsymbol{b}$ is then

$$\hat{\boldsymbol{b}} = (\boldsymbol{A}^\dagger \boldsymbol{W}^\dagger \boldsymbol{N}^{-1} \boldsymbol{W} \boldsymbol{A})^+ \boldsymbol{A}^\dagger \boldsymbol{W}^\dagger \boldsymbol{N}^{-1} \boldsymbol{W} \boldsymbol{v}_{\rm obs}, \qquad (24)$$

where M^+ denotes the Moore–Penrose pseudoinverse of a matrix M and $\boldsymbol{N} \equiv \langle \boldsymbol{n}\boldsymbol{n}^\dagger \rangle$ is the noise covariance matrix. Although we do not know the noise properties for the channels that are flagged, only the combination $\boldsymbol{W}^\dagger \boldsymbol{N}^{-1} \boldsymbol{W} \equiv \boldsymbol{N}_{\rm u}^{-1}$ appears in Equation (24). Here, we assume the noise at different frequency channels are independent of each other and write $\boldsymbol{N}_{\rm u}^{-1}$ as a diagonal matrix as follows

$$(\boldsymbol{N}_{\rm u}^{-1})_{kk} = \begin{cases} 1/\sigma^{\rm rms}(\nu_k)^2 & \text{if } \nu_k \text{ is unflagged} \\ 0 & \text{otherwise}, \end{cases} \qquad (25)$$

where $\sigma^{\rm rms}$ is given in Equation (16). Thus, the estimator $\hat{\boldsymbol{b}}$ depends solely on the information from unflagged frequency channels.

With these best-fitted DPSS coefficients, we can inpaint the flagged channels with the predicted foreground model. The entire inpainted visibility can thus be written as

$$\begin{aligned} \boldsymbol{v}_{\rm inp} &= \boldsymbol{W}\boldsymbol{v}_{\rm obs} + (\boldsymbol{I} - \boldsymbol{W})\boldsymbol{A}\hat{\boldsymbol{b}} \\ &= [\boldsymbol{W} + (\boldsymbol{I} - \boldsymbol{W})\boldsymbol{A}(\boldsymbol{A}^\dagger \boldsymbol{N}_{\rm u}^{-1} \boldsymbol{A})^+ \boldsymbol{A}^\dagger \boldsymbol{N}_{\rm u}^{-1}]\boldsymbol{v}_{\rm obs}. \end{aligned} \qquad (26)$$

For simplicity, we will denote the inpainting operator as $\mathcal{O}_{\rm inp}$ from here on. We note that the inpainted visibility is obtained with a completely linear operator on the observed visibility vector at a given time instance. The dashed blue lines in Figure 3 show the resulting power spectra if we inpaint over the flagged channels each night. Even though the simulated visibilities contained nightly varying systematic effects, we can see that our inpainting procedure is still able to reduce the discontinuities in the data and achieve the expected sensitivity.

4.2. Uncertainties in the Inpainted Data

While the empirical success of using inpainting to mitigate missing data due to RFI is demonstrated in Figure 3 and in the previous literature, one concern is how these data inpainting methods can affect the statistics of the 21 cm power spectrum as more and more channels are flagged. The uncertainties we choose to propagate are a subtle balance between formal statistical and practical considerations to which we devote some pedagogical discussion. Readers interested in the results can jump directly to Equation (34).

A typical error propagation technique when applying a linear operation to some data is to consider a frequentist thought experiment, where one repeatedly inpaints realizations of $\boldsymbol{v}_{\rm obs}$ with a fixed underlying signal, to obtain realizations of $\boldsymbol{v}_{\rm inp}$. This allows us to compute the covariance which will simply be

$\mathcal{O}_{\rm inp}\boldsymbol{N}_{\rm u}\mathcal{O}_{\rm inp}^\dagger$ with $\mathcal{O}_{\rm inp}$ defined in Equation (26).[32] To examine this form of covariance, let $\boldsymbol{P}_{\rm f}$ and $\boldsymbol{P}_{\rm u}$ be the projection operators on the flagged and unflagged channels, respectively. Then, on the unflagged channels, the uncertainties are

$$\boldsymbol{P}_{\rm u}\mathcal{O}_{\rm inp}\boldsymbol{N}_{\rm u}\mathcal{O}_{\rm inp}^\dagger \boldsymbol{P}_{\rm u}^\dagger = \boldsymbol{P}_{\rm u}\boldsymbol{N}_{\rm u}\boldsymbol{P}_{\rm u}^\dagger \equiv \boldsymbol{N}'. \qquad (27)$$

On the other hand, on the flagged channels, let $\mathcal{O}'_{\rm inp} \equiv \boldsymbol{P}_{\rm f}\boldsymbol{A}(\boldsymbol{A}^\dagger \boldsymbol{N}_{\rm u}^{-1} \boldsymbol{A})^+ \boldsymbol{A}^\dagger \boldsymbol{N}_{\rm u}^{-1}$ be the inpainting operation that maps the observed data $\boldsymbol{v}_{\rm obs}$ into a model, which we use to inpaint the flagged channels. The uncertainties on the flagged channels are

$$\boldsymbol{P}_{\rm f}\mathcal{O}_{\rm inp}\boldsymbol{N}_{\rm u}\mathcal{O}_{\rm inp}^\dagger \boldsymbol{P}_{\rm f}^\dagger = {}_{\rm inp}\boldsymbol{N}_{\rm u}{}_{\rm inp}^\dagger. \qquad (28)$$

We see that the uncertainties in the flagged channels correspond to a linear combination of uncertainties in the observed channels. Since there are usually significantly more unflagged data than flagged data, this results in a covariance matrix that often expresses more uncertainty in the unflagged data than in the flagged data. While this result is formally correct under the frequentist assumptions given above, as we propagate such a covariance matrix into our power spectrum estimation framework in Section 4.3, it has the uncomfortable side effect of giving more weight to inpainted solutions in the flagged channels than the actual measured data in the unflagged channels.

If we cast inpainting as an inference problem, there is an alternative Bayesian formulation in terms of the posterior predictive distribution, $P(\boldsymbol{v}'|\boldsymbol{v}_{\rm obs}, \boldsymbol{N}, \boldsymbol{A})$, that does not have this undesirable property. Here, $\boldsymbol{v}'$ is the hypothetical unobserved RFI-free visibility in the flagged channels including the thermal noise that would corrupt it, and $\boldsymbol{v}_{\rm obs}$ is the observed visibility.[33] As before, $\boldsymbol{N}$ is the full frequency–frequency noise covariance and $\boldsymbol{A}$ is the design matrix of a given basis that maps a set of coefficients $\boldsymbol{b}$ to a foreground shape in the frequency space. In Bayesian inference, probability is an extension of Boolean logic where propositions may be ascribed an uncertainty rather than a strict binary truth value. The posterior predictive distribution answers the question, "Given some known prior information, including a model that is assumed to *completely* describe the processes in the data, and some observed data, what is the probability (density) that some unobserved data lie in the (infinitesimal) interval $[\boldsymbol{v}''_{\rm inp}, \boldsymbol{v}'_{\rm inp} + d\boldsymbol{v}'_{\rm inp}]$?"

The posterior predictive distribution can be calculated by marginalizing over $\boldsymbol{b}$ as follows

$$\begin{aligned} &P(\boldsymbol{v}'|\boldsymbol{v}_{\rm obs}, \boldsymbol{N}, \boldsymbol{A}) \\ &= \int d\boldsymbol{b}\, P(\boldsymbol{v}'_{\rm inp}|\boldsymbol{b}, \boldsymbol{N}'_{\rm f}, \boldsymbol{A})P(\boldsymbol{b}|\boldsymbol{v}_{\rm obs}, \boldsymbol{N}_{\rm u}, \boldsymbol{A}), \end{aligned} \qquad (29)$$

where we use $\boldsymbol{N}_{\rm u}$ to denote the noise covariance of the observed data and $\boldsymbol{N}' \equiv \boldsymbol{P}_{\rm f}\boldsymbol{N}\boldsymbol{P}_{\rm u}^\dagger$ for the noise variance of the hypothetical RFI-free data in the flagged channels. While $\boldsymbol{N}_{\rm u}$ can be

---

[32] While strictly speaking, $\boldsymbol{N}_{\rm u}^{-1}$ as defined by Equation (25) has no inverse, the infinite variance in the flagged channels in $\boldsymbol{N}_{\rm u}$ does not affect our calculations as it is always projected out.

[33] We note that unlike in the previous subsection where $\boldsymbol{v}_{\rm inp}$ is a vector with dimension $N_{\rm freq}$, $\boldsymbol{v}''_{\rm inp}$ now has dimension $N_{\rm freq,flagged}$. This is because, by construction, we only inpaint data and predict a solution for the visibility in the flagged channel. Therefore, in the Bayesian approach, we are only interested in the probability distribution of the underlying visibility in the unobserved channels given the observed data.

estimated using the autocorrelations as in Equation (25), we do not know N', i.e., the noise properties in the flagged channels, a priori. However, since the autocorrelations are very smooth, we can safely assume that we can interpolate the autocorrelations over the flagged channels and infer N' with very low uncertainty.

The two factors in the integrand of Equation (29) are the intrinsic uncertainties in the flagged channels, conditioning on an underlying signal predicted by b, and the uncertainties in the signal model b itself. The two terms can be written as

$$P(v'|b, N'_f, A)$$
$$\propto \exp\left[-(v' - P_f A b)^\dagger N'^{-1}_f (v' - P_f A b)\right], \quad (30)$$

and assuming a flat prior on b,

$$P(b|v_{obs}, N_u, A) \propto P(v_{obs}|b, N_u, A) P(b)$$
$$\propto \exp\left[-(v_{obs} - A b)^\dagger N_u^{-1} (v_{obs} - A b)\right]. \quad (31)$$

Note that the maximum likelihood estimator $\hat{b}$ given in Equation (24) is where $\partial P(b|v_{obs}, N_u, A)/\partial b = 0$. We show in the Appendix that integrating Equation (29) gives

$$P(v'|v_{obs}, N, A) \propto$$
$$\exp\left[-(v' - P_f A \hat{b})^\dagger N'^{-1}_{inp} (v' - P_f A \hat{b})\right], \quad (32)$$

where

$$N'_{inp} \equiv (N'_f + \mathcal{O}' N_u \mathcal{O}'^\dagger). \quad (33)$$

We therefore see that the uncertainties in the inpainted channels indeed come from two sources: (1) the intrinsic noise uncertainties in these channels described by N'_f; (2) the posterior uncertainties associated with inferring v' from v_{obs}. We note that the second term here is exactly the same as the uncertainties on the flagged channels from the frequentist approach. Since each element of N'_f is similar to that of N_u, the combination of the frequentist uncertainties with N'_f means that the inpainted data will have larger uncertainties than the unflagged data in our new formalism.

To generalize this to a full frequency–frequency covariance for inpainted visibility v_{inp}, we propose the following modification to the frequentist covariance

$$N_{inp} \equiv (N_f + \mathcal{O}_{inp} N_u \mathcal{O}^\dagger_{inp}). \quad (34)$$

This form of the covariance matrix has several desirable qualitative features. It has the full posterior predictive distribution's uncertainty in addition to the correlations between the inpainting solution and any noise affecting the data used for inference. It does not give more weight to the (highly incomplete) model predictions in the flagged channels. In the absence of any flagging, it reduces to the standard error propagation procedure, which is to just propagate the thermal noise variances.

We note that in a fully Bayesian treatment, we would propose a model that fully describes the observed data to the best of our ability, and there would be no essential need to consider the relationship between the flagged and unflagged data. One would summarize the unknown values of the model parameters using the posterior distribution conditioning on the observed data and pass this forward to power spectrum
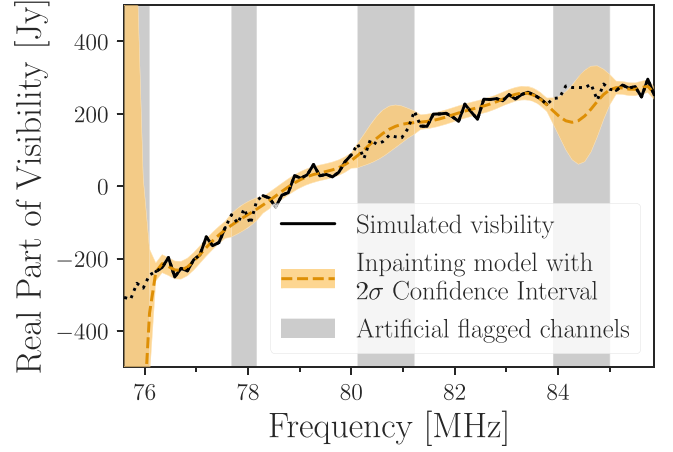

Figure 4. Uncertainties in the inpainted visibilities for various types of flagged channels. The solid black line is the simulated visibility at a single time instance at a single night from a single 14.6 m baseline. We flag the simulated visibility with two five-channel-wide gaps on the left and two 10-channel-wide gaps on the right (shaded gray region). The dashed orange line shows the best-fit inpainted model with the 2σ uncertainties given in the shaded region. This can be compared with the dotted black line which represents the underlying true simulated visibility in the flagged region.

estimation (F. Kennedy et al. 2023; J. Burba et al. 2024). For inpainting, however, we choose a model only to smooth out spectral irregularities from RFI flags in order to generate the power spectrum under the quadratic estimator framework (see Section 4.3). Our model is deliberately chosen to be incomplete in a very critical way: it has essentially no structure beyond some delay by construction. We therefore do not choose the fully Bayesian approach but explore this alternative approach by framing the process of inpainting into an inference problem and extracting the correlation between the inpainting solution and the observed data. In Section 4.3, we will utilize the result derived here to incorporate the effect of inpainting into our power spectrum quadratic estimator.

Figure 4 shows the performance of our inpainting method across flags with different widths at different locations of the band. The solid black line is the simulated visibility at a single time instance at a single night from a single 14.6 m baseline. We flag the simulated visibility with two five-channel-wide gaps on the left and two 10-channel-wide gaps on the right. The dashed orange line shows the best-fit inpainted model $A\hat{b}$. The uncertainties indicated by the shaded region are given by $\sigma(\nu_i) = \sqrt{(N'_f + \mathcal{O}'_{inp} N_u \mathcal{O}'^\dagger_{inp})_{ii}/2}$, where the factor of 2 comes from the fact that we are looking only at the uncertainties in the real part of the visibility. Compared to the true underlying visibility (solid black line), we can clearly see that the inpainting models are less constrained across larger gaps or gaps near the edge of the spectral window. While the best-fit inpainting model can be highly biased in these cases, we stress that the final goal of inpainting is to smoothly connect signals in the visibility space to enable us to generate a power spectrum free from the bright foreground ringing. Thus, the success of the inpainting method needs to be examined in the power spectrum space, which we will discuss next.

4.3. Impact on Power Spectrum Covariance

While the inpainted visibility might not perfectly recover the true data, the primary goal of inpainting is merely to smoothly connect gaps in the visibility space without introducing the

bright foreground ringing in the power spectrum estimator. Therefore, the most important quantity to examine is the statistical impact of inpainting on the power spectrum estimator. Here, we focus on the delay power spectra derived under the quadratic estimator (A. Liu & M. Tegmark 2011; A. R. Parsons et al. 2014) formalism. Here, we give a brief summary of the delay power spectra estimator and the evaluation of its statistical properties.

A per-baseline quadratic estimator $\hat{P}$ of the αth band power of the 21 cm delay power spectrum can be written as

$$\hat{P}_\alpha \equiv \boldsymbol{v}^\dagger \boldsymbol{E}_\alpha \boldsymbol{v}, \tag{35}$$

where $\boldsymbol{v}$ is the visibility vector, and $\boldsymbol{E}$ is chosen by the analyst. For simplicity, we consider an estimator that performs a straightforward discrete Fourier transform.

$$\boldsymbol{E}_\alpha \equiv M_{\alpha\beta} \boldsymbol{R}^\dagger \boldsymbol{Q}^{\mathrm{DFT},\beta} \boldsymbol{R}, \tag{36}$$

where $Q_{ij}^{\mathrm{DFT},\beta} = e^{2\pi i \tau_\beta(\nu_i - \nu_j)}$ does the delay transform. Here, we choose $R_{ij} = \gamma(\nu_i)\delta_{ij}$ to be just a tapering matrix, and $M_{\alpha\beta}$ is the normalization factor, which will be specified later.

The expectation value of the estimator is

$$\langle \hat{P}_\alpha \rangle = \mathrm{tr}[\boldsymbol{E}_\alpha \boldsymbol{C}], \tag{37}$$

where $\boldsymbol{C} \equiv \langle \boldsymbol{v}\boldsymbol{v}^\dagger \rangle$ is the data covariance matrix. In general, we can decompose the data covariance into

$$\boldsymbol{C} = \boldsymbol{C}_{\mathrm{sig}} + \boldsymbol{N}, \tag{38}$$

where $\boldsymbol{N}$ is the noise covariance and $\boldsymbol{C}_{\mathrm{sig}}$ represents the signal covariance from both the foreground sky emission and the cosmological 21 cm signal. Using Equation (1), the signal covariance can be written as

$$(\boldsymbol{C}_{\mathrm{sig}})_{ij} = \langle V_{\boldsymbol{b}}(\nu_i) V_{\boldsymbol{b}}^*(\nu_j) \rangle$$
$$= \int d\eta d^2\boldsymbol{u}\, P(\boldsymbol{u}, \eta) \times [$$
$$\tilde{B}(\boldsymbol{u_b} - \boldsymbol{u}, \nu_i)\tilde{B}^*(\boldsymbol{u_b} - \boldsymbol{u}, \nu_j)e^{i2\pi\eta(\nu_i-\nu_j)}]$$
$$\approx \int d\eta\, P(\boldsymbol{u_b}, \eta)e^{i2\pi\eta(\nu_i-\nu_j)} \times [$$
$$\int d^2\boldsymbol{u}\, \tilde{B}(\boldsymbol{u_b} - \boldsymbol{u}, \nu_i)\tilde{B}^*(\boldsymbol{u_b} - \boldsymbol{u}, \nu_j)]$$
$$\approx \sum_\alpha \bar{P}_\alpha \Delta\eta e^{i2\pi\eta_\alpha(\nu_i-\nu_j)}\int d^2\boldsymbol{\theta}B(\boldsymbol{\theta}, \nu_i)B^*(\boldsymbol{\theta}, \nu_j)$$
$$\equiv \sum_\alpha \bar{P}_\alpha \frac{\partial \boldsymbol{C}_{\mathrm{sig}}}{\partial P_\alpha}, \tag{39}$$

where η and $\boldsymbol{u}$ is the Fourier dual of frequency ν and spatial coordinate $\boldsymbol{\theta}$, respectively, $P(\boldsymbol{u}, \eta)$ is the true signal power spectrum, $\bar{P}_\alpha$ represents the averaged band power within a narrow bin of η, and $\tilde{B}(\boldsymbol{u}, \nu_i)$ is the spatial Fourier transform of the antenna primary beam profile which we assume to be relatively compact as a function of $\boldsymbol{u}$. Therefore,

$$\langle \hat{P}_\alpha \rangle = \sum_\beta \mathrm{tr}\left[\boldsymbol{E}_\alpha \frac{\partial \boldsymbol{C}_{\mathrm{sig}}}{\partial P_\beta}\right]\bar{P}_\beta + \mathrm{tr}[\boldsymbol{E}_\alpha \boldsymbol{N}]$$
$$\equiv \sum_\beta W_{\alpha\beta}\bar{P}_\beta + b_\alpha. \tag{40}$$

Here, $W_{\alpha\beta}$, often called the window function (A. Liu & M. Tegmark 2011; A. Gorce et al. 2023), represents the connection between the power spectrum estimator and the underlying true power spectrum. b_α is the noise bias in our

estimator, which can either be subtracted by the analyst or can be avoided by forming an estimator using visibilities from different times (a technique known as *time interleaving*; J. Tan et al. 2021). The normalization matrix $M_{\alpha\beta}$ can now be chosen such that the window function is power-conserving, i.e.,

$$\sum_\beta W_{\alpha\beta} = 1. \tag{41}$$

Meanwhile, the covariance of the power spectrum estimator can be obtained as (J. Tan et al. 2021)

$$\Sigma_{\alpha\beta} \equiv \langle \hat{P}_\alpha \hat{P}_\beta^\dagger \rangle - \langle \hat{P}_\alpha \rangle \langle \hat{P}_\beta^\dagger \rangle$$
$$= \mathrm{tr}[\boldsymbol{E}_\alpha \boldsymbol{C}_{\mathrm{sig}}\boldsymbol{E}_\beta \boldsymbol{N} + \boldsymbol{E}_\alpha \boldsymbol{N}\boldsymbol{E}_\beta \boldsymbol{C}_{\mathrm{sig}} + \boldsymbol{E}_\alpha \boldsymbol{N}\boldsymbol{E}_\beta \boldsymbol{N}], \tag{42}$$

where we have ignored the contribution from cosmic variance. We note that the power spectrum covariance here includes the signal-noise cross terms that are important in the signal-dominated regime (M. Kolopanis et al. 2019; J. Tan et al. 2021).

To include the impact of data inpainting, we can substitute the data covariance matrix to the covariance of the inpainted visibility $\boldsymbol{v}_{inp} = \mathcal{O}_{inp}\boldsymbol{v}_{obs}$. Naively, the covariance of the inpainted visibility is therefore

$$\boldsymbol{C}^{\mathrm{inp}} = \mathcal{O}_{\mathrm{inp}}\langle \boldsymbol{v}_{\mathrm{obs}}\boldsymbol{v}_{\mathrm{obs}}^\dagger \rangle \mathcal{O}_{\mathrm{inp}}^\dagger$$
$$= \mathcal{O}_{\mathrm{inp}}\boldsymbol{C}_{\mathrm{sig}}\mathcal{O}_{\mathrm{inp}}^\dagger + \mathcal{O}_{\mathrm{inp}}\boldsymbol{N}\mathcal{O}_{\mathrm{inp}}^\dagger. \tag{43}$$

However, as discussed in Section 4.2, the term $\mathcal{O}_{\mathrm{inp}}\boldsymbol{N}\mathcal{O}_{\mathrm{inp}}^\dagger$ only captures the uncertainties in the inpainted model due to the noise in the unflagged channels but does not fully capture the intrinsic uncertainties associated with the flagged channels if we were to observe them. In other words, even if the inpainting model can be determined perfectly, there should still be a term that corresponds to the uncertainties due to thermal noise so that inpainting does not artificially increase our sensitivity. Therefore, we model the data covariance after inpainting as

$$\boldsymbol{C}^{\mathrm{inp}} = \mathcal{O}_{\mathrm{inp}}\boldsymbol{C}_{\mathrm{sig}}\mathcal{O}_{\mathrm{inp}}^\dagger + \mathcal{O}_{\mathrm{inp}}\boldsymbol{N}_{\mathrm{u}}\mathcal{O}_{\mathrm{inp}}^\dagger + \boldsymbol{N}_f. \tag{44}$$

Here, we define $\boldsymbol{C}_{\mathrm{sig}}^{\mathrm{inp}} \equiv \mathcal{O}_{\mathrm{inp}}\boldsymbol{C}_{\mathrm{sig}}\mathcal{O}_{\mathrm{inp}}^\dagger$ and $\boldsymbol{N}^{\mathrm{inp}} \equiv \mathcal{O}_{\mathrm{inp}}\boldsymbol{N}_{\mathrm{u}}\mathcal{O}_{\mathrm{inp}}^\dagger + \boldsymbol{N}_f$. We note that Equation (44) denotes the covariance of inpainted visibility at a single time instance and a single night of observation. In practice, we coherently average the inpainted visibility $\boldsymbol{v}_{\mathrm{inp}}^{\mathrm{tavg}}$ across different sidereal days and within a 300 s window before making the power spectrum. Since the flagging pattern can be different from time to time, inpainting is thus a time-varying operation. The covariance for the time-averaged visibility vector is then

$$\mathrm{Cov}(\boldsymbol{v}_{\mathrm{inp}}^{\mathrm{tavg}}, \boldsymbol{v}_{\mathrm{inp}}^{\mathrm{tavg}}) = \frac{1}{n_{\mathrm{night}}^2 n_{\mathrm{coherent}}^2}\Big[\sum_{ij}\mathcal{O}_{\mathrm{inp},i}\boldsymbol{C}_{\mathrm{sig}}\mathcal{O}_{\mathrm{inp},j}^\dagger$$
$$+ \sum_i \mathcal{O}_{\mathrm{inp},i}\boldsymbol{N}_{\mathrm{u},i}\mathcal{O}_{\mathrm{inp},i}^\dagger + \boldsymbol{N}_{f,i}\Big], \tag{45}$$

where n_{night} is the number of nights we observe, n_{coherent} is the amount of data samples within a 300 s window, and the index i and j run through all the times and days we average over.

Figure 5 shows the noise (co)variance of the inpainted visibility calculated through the last two terms in Equation (45). Here, the visibility is from a single 14.6 m baseline in our simulation after coherently averaging across sidereal days and a 300 s window. The percentage of unflagged data as a function of the frequency can be seen in the top panel of Figure 5. The variance and the covariance of the inpainted visibility are given as the solid black
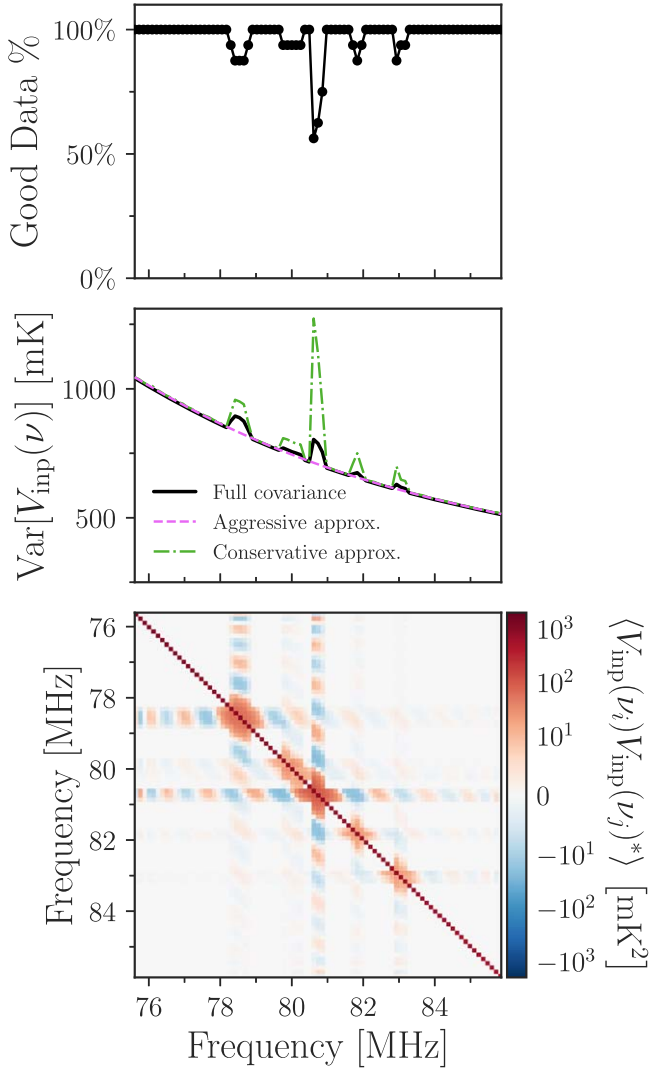
Figure 5. Statistics of inpainted data in the visibility domain in our simulation. Top: overall percentage of good data in the simulation as a function of the frequency. The results presented here are for a single 14.6 m baseline at a single time instance after coherently averaging across sidereal days and a 300 s window. Center: estimates of the noise variance in the inpainted visibility from a full-covariance treatment (solid black) and two different approximations (dashed and dashed–dotted). Bottom: frequency–frequency noise covariance matrix including the effect of inpainting obtained from the last two terms in Equation (45).

line in the middle panel and the bottom panel, respectively. We can see that at the frequency range where there is no flagged channel (i.e., 100% good data), the noise covariance is completely diagonal and simply follows N_u. Meanwhile, inpainting introduces a correlation between the flagged channel and the unflagged channel which can be clearly seen in the bottom panel of Figure 5.

Unfortunately, it might not always be computationally feasible to propagate the full-covariance matrix. One simplification one could make is to ignore the off-diagonal correlation and develop an approximation for the variances. For completely unflagged channels, the variances are estimated with the radiometer equation combined with the antenna's autocorrelation

$$\sigma_{ij}^2(\nu) = \frac{V_{ii} V_{jj}}{N_{\text{sample}} \Delta\nu \Delta t}, \qquad (46)$$

where N_{sample} traces the amount of data we coherently combined, in this case, $n_{\text{night}} \times n_{\text{coherent}}$. For channels with flagged data, there are intuitively two ways to assign N_{sample}. One is to assume we have perfectly predicted the signal in the flagged channels through inpainting, and these flagged channels contain as much information as other unflagged channels. This is the same as assuming the noise covariance is just $N_u + N_f$, and ignoring the uncertainties in inpainting. The variance predicted by this approach is shown as the dashed magenta curve in the middle panel of Figure 5. A more conservative approach is to assume that the flagged channels contain no information at all even after inpainting. This can be achieved by modifying the N_{sample} parameter and assuming flagged channels do not contribute to N_{sample}. The variance calculated from this approach is given in dashed–dotted green. In reality, inpainted channels do contain some information inferred from the neighboring channels. We see that the variance calculated by propagating the full-covariance matrix lies in between the two approximations.

Figure 6 shows the delay power spectrum from the inpainted visibility and various power spectrum statistics discussed above. The solid black line in the top panel shows the power spectrum for the same inpainted visibility presented in Figure 5. The three dotted lines show the error in the power spectrum estimator obtained by using three different forms of noise covariance for the inpainted visibility in Equation (42). Here, the error power spectrum P_{SN} is defined to be the square root of the diagonal terms of the full power spectrum covariance (J. Tan et al. 2021), i.e.,

$$P_{\text{SN}}(k_\alpha) \equiv \sqrt{\Sigma_{\alpha\alpha}} , \qquad (47)$$

where $\Sigma_{\alpha\beta}$ is given in Equation (42). The dotted black line is obtained by using the full noise covariance given by Equation (45), while the two colored lines are from the two approximations discussed above. We see that while the variance of inpainted visibility in the frequency space is bounded by our two approximations as shown in Figure 5, the off-diagonal terms in the full frequency–frequency covariance matrix make the resulting uncertainties in the power spectrum space higher than either one of our approximations. In the case where not a significant amount of data are flagged, we see that the conservative approach (dotted green, which assumes inpainted data do not contribute to the N_{sample} in the noise estimate in Equation (46)) gives a reasonable approximation to the error obtained by propagating the full-covariance matrix. Scenarios where this ceases to be true will be discussed in Section 5.2.

The lower panel of Figure 6 shows the window functions for the delay power spectrum estimator at different delay bins. The solid gray lines in the background are the window functions obtained without including the effect of inpainting, i.e., using Equations (40) and (39). To include the effect of inpainting, following Equation (45), the window functions become

$$W_{\alpha\beta}^{\text{inp}} = \frac{1}{n_{\text{night}}^2 n_{\text{coherent}}^2} \sum_{ij} \text{tr}\left[E_\alpha \mathcal{O}_{\text{inp},i} \frac{\partial C_{\text{sig}}}{\partial P_\beta} \mathcal{O}_{\text{inp},j}^\dagger \right], \qquad (48)$$

where the index i and j run through all the times and days we average over. The resulting window functions are shown as the colored lines in the lower panel of Figure 6. Here, the
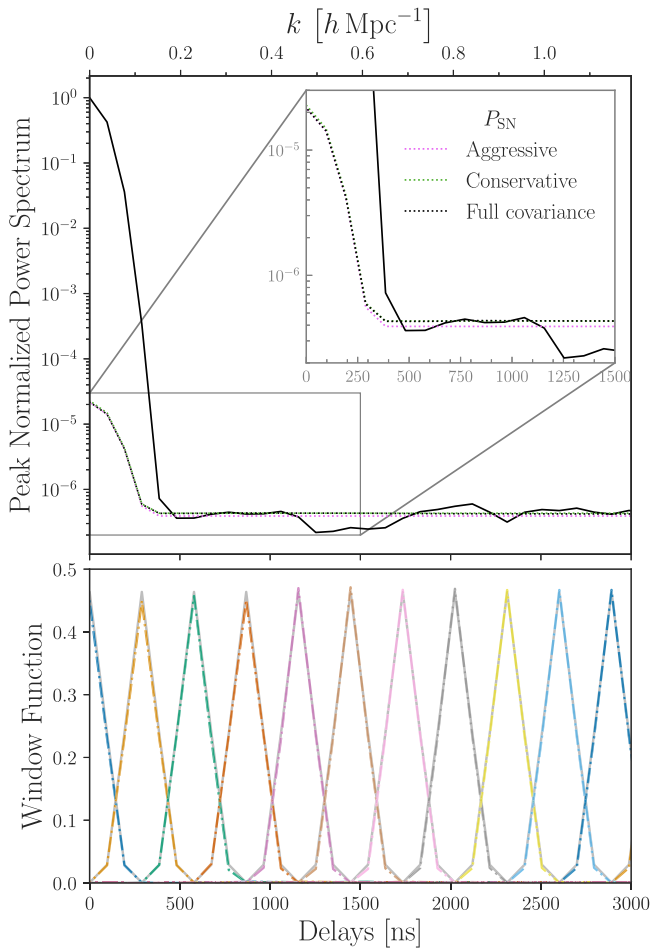
Figure 6. Delay power spectrum and power spectrum window function from inpainted visibility in our simulation. The delay spectrum is obtained with the inpainted visibility of a single 14.6 m baseline after coherently averaging across sidereal days and a 300 s window. The delay spectrum is further averaged incoherently within a 1.5 hr window. Top: delay power spectrum (solid black) and error estimates (dotted lines). The three dotted lines correspond to power spectrum error bars calculated with different inpainted noise covariance matrices as in Figure 5. Bottom: power spectrum window function obtained through Equation (40). The gray lines show the window functions if we ignore the effect of inpainting while the color dashed lines include the impact of inpainting using Equation (48).

difference between including and not including a proper treatment of the effect of inpainting is small as not a large percentage of data are flagged. The effect of inpainting on window functions will be further examined in Section 5.2.

5. Application to HERA

Equipped with the intuition and statistical tools from the previous sections, in this section we discuss the application to the Phase II data obtained by HERA. HERA is a drift-scan EoR experiment with 350 parabolic 14 m dishes located in the Karoo desert in South Africa. HERA Phase II involves an upgrade to the Vivaldi feeds that allows for observations in a wider frequency range from 50 to 250 MHz. In Section 5.1, we introduce a small set of HERA Phase II observations taken in 2022 October. Detailed strategies for inpainting and results are given in Section 5.2.

5.1. Data and Flags

The first season of scientific observation for HERA Phase II began in 2022 October. A preliminary analysis of the first 14

nights of high-quality observations was performed. While over 170 antennas were constructed at the time, only ~90 were producing good data passing various stringent antenna metrics.

The data presented here have passed through multiple stages of analyses in order to properly calibrate the data and detect RFI. The calibration strategy adopted here is similar to the HERA Phase I analyses (Z. Abdurashidova et al. 2022; HERA Collaboration et al. 2023). The RFI flagging pipeline has been upgraded in the Phase II analysis to better capture time-varying broadband RFI that are likely the results of lightning. The details of the RFI identification routine are documented in the HERA Team Memos (J. Dillon & S. Murray 2023; S. Murray et al. 2023; J. Dillon et al. 2024); here we give a brief summary of the RFI flagging process.

In general, RFI in the HERA data are identified through a combination of different metrics to isolate the outliers. For the data presented here, two types of flags are created. The first is an antenna flag where we flag bad antenna polarization across the band. These flags are created on a nightly basis, first for every two integration times, and later harmonized so that we continuously flag an antenna across a large period if it is flagged for a significant percentage of times within. The second type of flag is an array-wide RFI mask. These flags are created nightly by identifying misbehaving time and frequency channels in the array-averaged autocorrelation functions and cross-correlation functions. Such a mask can capture low-level RFI as they can only be seen after we average down the data to increase sensitivity.

Figure 7 shows the amount of good data for the shortest east–west baseline group across 14 nights of observations. For the remainder of this section, we focus on the data below the FM radio band, which was previously inaccessible by the Phase I instruments. The low-band data offer a unique opportunity to observe deep into the cosmic dawn but also present significant challenges due to the brighter foreground contamination. Mitigating any potential leakage of bright foreground modes is therefore even more crucial at this frequency range.

5.2. Inpainting Strategies and Results

Following the methodology outlined in Section 4.1, the HERA data are inpainted with a DPSS basis localized within ± 500 ns in the Fourier space. As we discussed in Section 4.1, we choose 500 ns so that the DPSS basis not just captures the bright foreground modes within the wedge, but also any potential foreground leakage due to systematic effects. While this does mean that we are inpainting into the EoR window for some baselines, the formalism developed in Section 4 makes sure that we are able to accurately take into account the impact of inpainting in these delay ranges. To reduce the uncertainties in inpainting, we fit the DPSS basis to all the data points below the FM radio band (A. Ewall-Wice et al. 2021; N. S. Kern & A. Liu 2021). Following this inpainting step, we select a 12 MHz frequency window (marked in green in Figure 7) to examine the power spectrum.

To demonstrate the necessity of data inpainting, we calculate the delay power spectra within this frequency window with or without inpainting in Figure 8. The power spectra are derived from 14 nights of data observed by all the 14.6 m east–west baselines with a 300 s coherent time average and a 1.5 hr incoherent time average. Similar to what we have already seen from the simulation, the delay spectrum from the inpainted
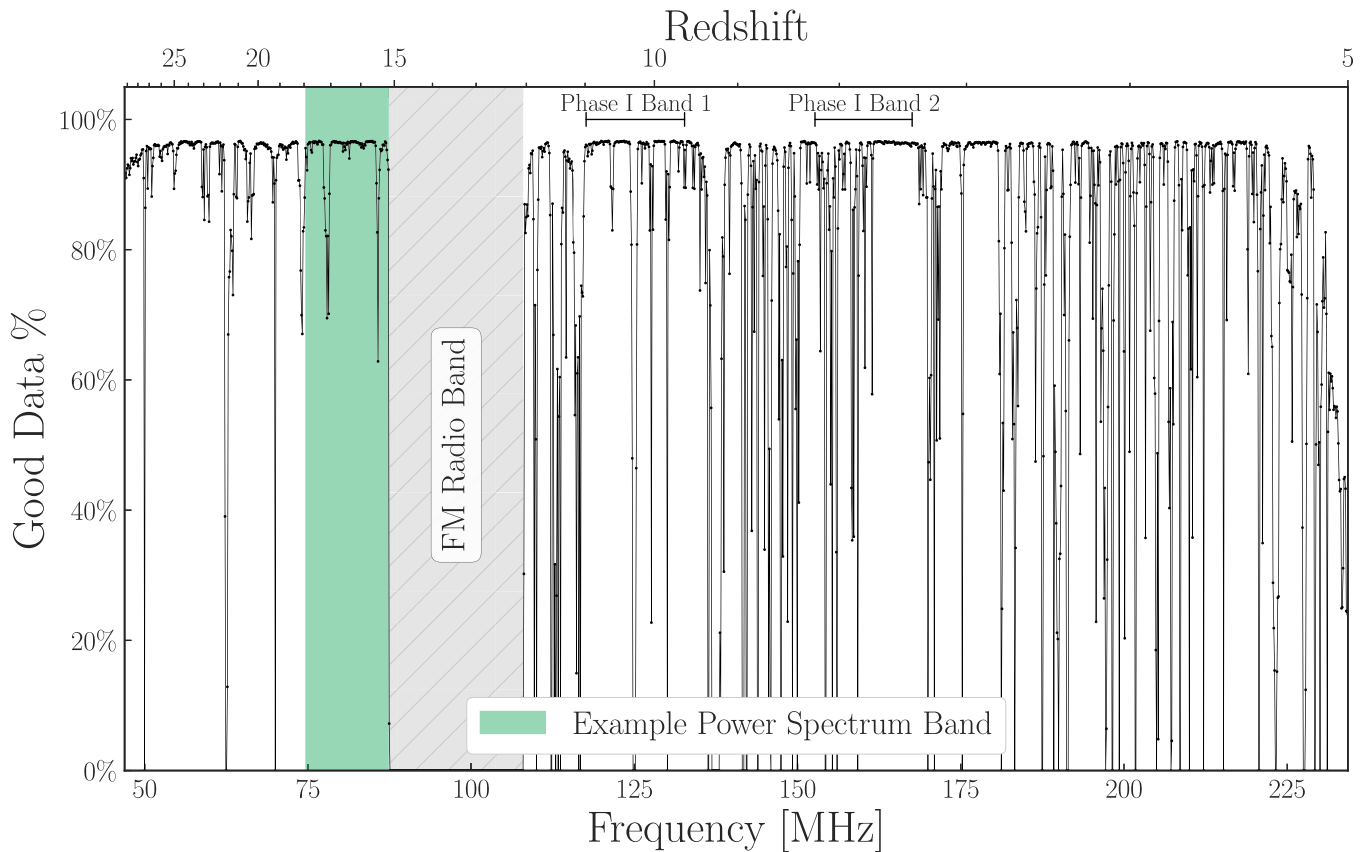
Figure 7. Percentage of good data for the shortest east–west baseline group across 14 nights of observations with the HERA Phase II instruments. The upgraded Vivaldi feed extends our observation range roughly from 50 to 250 MHz. The gray region is excluded due to heavy contamination from FM radio. The 12 MHz wide frequency range, which we use to derive sample power spectra, is marked in green.

visibility (solid blue) agrees well at high delay with the expected sensitivity obtained through the radiometer equation (dotted black). Meanwhile, even though every frequency channel within this band of interest has at least 60% good data, we see that the resulting power spectrum (dashed orange) from directly averaging the visibilities across sidereal day exhibits significant leakage of bright foreground modes. The result without inpainting is more than one order of magnitude away from the expected noise floor. This demonstrates two points: (1) nightly varying systematic effects exist in the HERA Phase II data, and (2) inpainting over gaps due to RFI on a nightly basis is necessary to reduce the interplay between flags and systematic effects. We note that we also observe deviation from the expected noise level at a lower delay ($\leqslant 1000$ ns) even when inpainting is performed. This is due to other systematic effects such as instrument coupling (N. S. Kern et al. 2019; A.T. Josaitis et al. 2022; E. Rath et al. 2024) and can be mitigated with additional analysis steps (N. S. Kern et al. 2019; H. Garsden et al. 2024; R. Pascua et al. 2024). These additional systematic mitigation strategies are not employed here for simplicity.

Figure 9 shows the power spectrum from the nightly inpainted HERA Phase II data together with all the statistical quantities discussed in Sections 4.2 and 4.3. Similar to Figure 5, the panels on the left-hand side show the properties of the inpainted visibility in the frequency space. The lower-left panel shows the frequency–frequency noise covariance matrix after inpainting following Equation (45) while the variance is shown as the solid black line in the middle panel. An
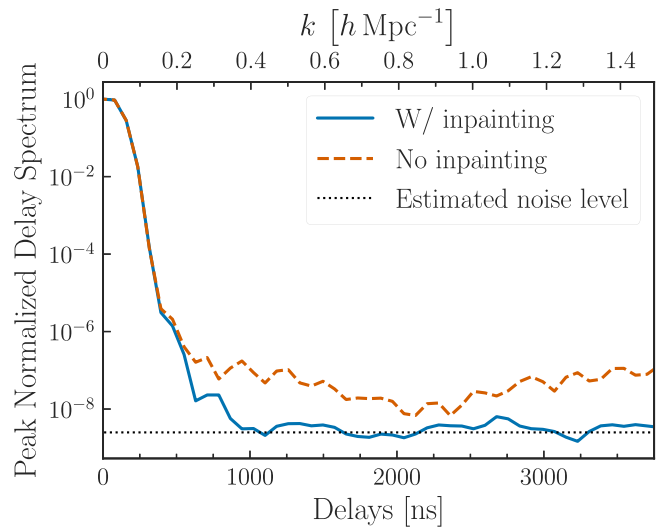
Figure 8. Delay power spectra from the H6C Phase II data with (solid blue) or without (dashed orange) nightly inpainting. The power spectra are derived from 14 nights of data observed by all the 14.6 m east–west baselines with a 300 s coherent time average and a 1 hr incoherent time average. The frequency range where the power spectra are derived and the RFI flagging pattern in the data can be seen in the green band in Figure 7. The expected sensitivity for these data obtained through the radiometer equation is given in the dotted line.

approximation to the variance from the full-covariance matrix is given in the dashed–dotted green line. This is the *conservative* approximation shown in Figure 5 as it has been
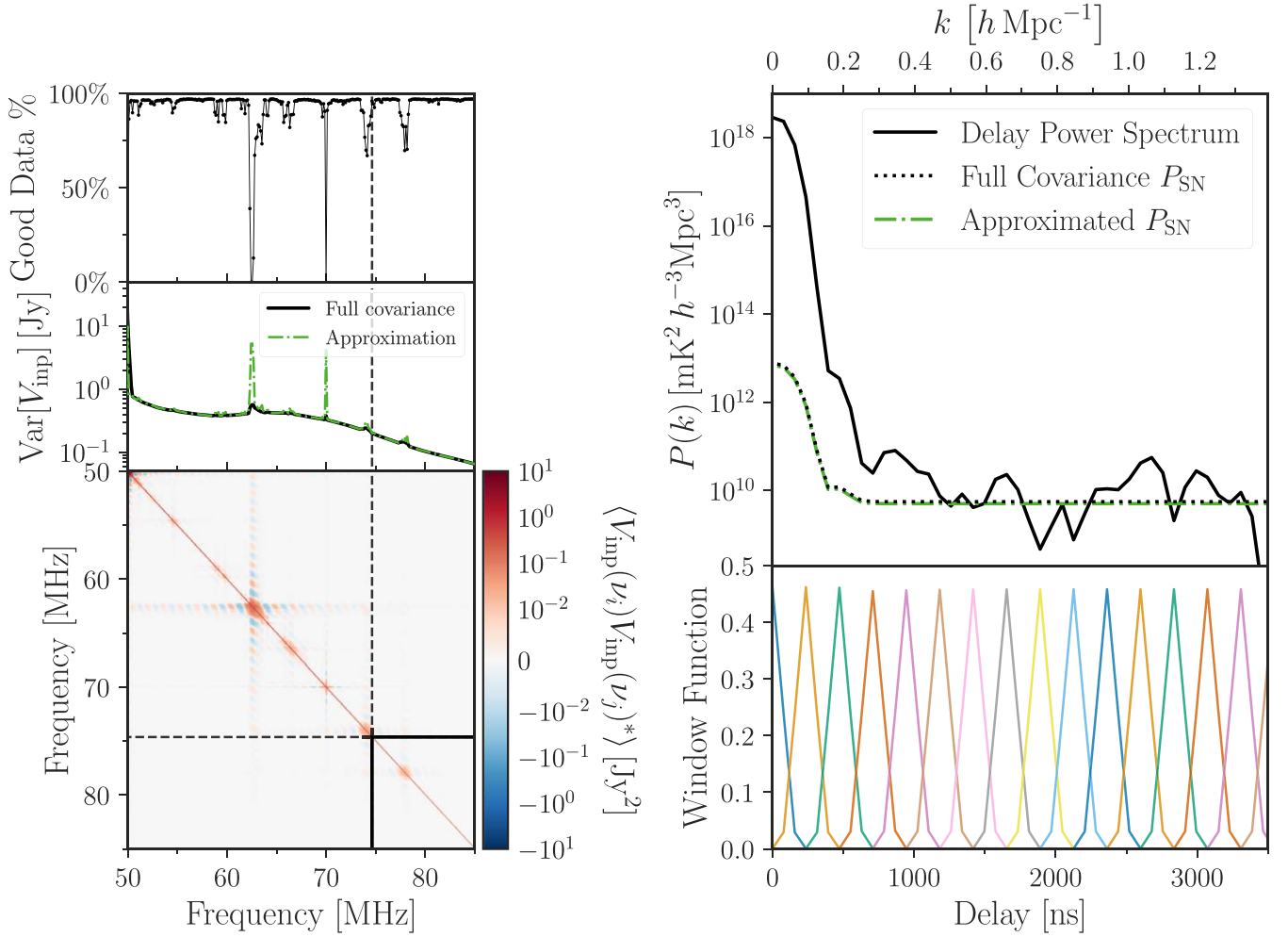
Figure 9. Statistical properties of nightly inpainted visibility from the HERA Phase II data. Similar to Figure 8, the results shown here are derived from data observed by all the 14.6 m east–west baselines in the array. The visibility is coherently averaged across 14 nights of observations and a 300 s window. Left: statistical properties in the frequency space including flagging ratio and (co)variance of the inpainted visibility data. Right: statistical properties in the Fourier space including delay power spectrum, power spectrum error estimate, and the window function.

shown to better approximate the power spectrum error bar in Figure 6. We note that for the conservative approximation, we assign N_{sample} in Equation (46) using only the number of unflagged channels. Here, for channels that are completely flagged across all nights, we take N_{sample} to be the smallest positive number across the band to avoid dividing by zero in Equation (46).

The right two panels of Figure 9 show the resulting power spectrum and various power spectrum statistics for the nightly inpainted HERA Phase II data. We note that the power spectra are derived from a subset of the frequency range where we inpaint the data. All the power spectrum statistics shown here are derived with the covariance matrix projected to the frequency subspace where we calculate the power spectrum estimator. We see that in the presence of only a small fraction of flagged data, the approximated P_{SN} agrees well with P_{SN} derived from the full frequency–frequency covariance, and the effect of inpainting on the window function is also negligible.

However, as we inpaint over more data or over larger gaps, our proposed approximation might not be able to faithfully capture the impact of inpainting on power spectrum statistics. To determine the cases where the effect of inpainting is no longer statistically negligible, we artificially inject flags of different widths into the observed data. To maximize the effect

of missing data, we position the flag at the center of the frequency band where we derive the power spectrum (~81 MHz). Figures 10 and 11 show the resulting changes in power spectrum statistics as a function of the flagged channel width. In Figure 10, we introduce flags with different widths in 1 out of the 14 nights of data while flags are introduced every night in Figure 11.

The top panels of Figures 10 and 11 show the delay power spectra (solid lines) and error estimates (dotted lines) derived from the full covariance of the inpainted visibility. We see that as the width of the injected flag increases, especially when flagging over all 14 nights, the amplitude of the power spectrum decreases at lower delays. This is because of the correlation introduced by inpainting. Inpainting over large gaps causes the low-delay modes to correlate strongly with high-delay modes. The power at lower delays is thus diluted as we are measuring a weighted average of the intrinsic power at low and high delays. It is therefore important to carefully take the power spectrum window function into account when interpreting data with a significant amount of flags.

Meanwhile, the ratio between the full-covariance error estimates and the approximation is given in the second panel of Figures 10 and 11. In the case where only 1 out of the 14 nights is flagged, our approximated error estimates always
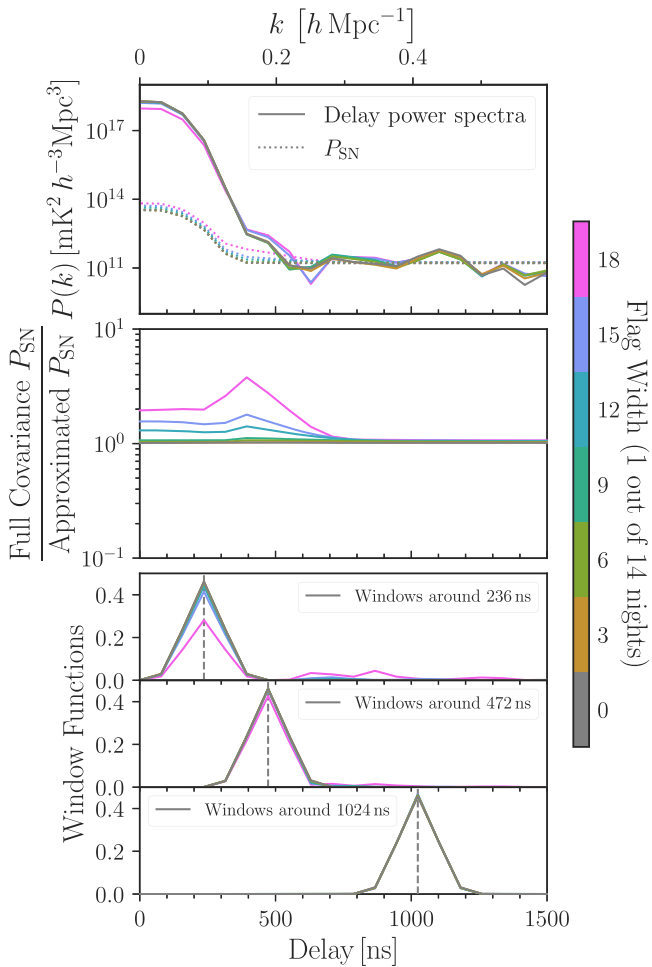
Figure 10. Changes in power spectrum statistics as a function of the flagged channel width. Here, we artificially flag channels in 1 of the 14 nights in the observed HERA Phase II data and inpaint over them to investigate the impact of inpainting over gaps with different widths. The flagged channels are placed contiguously at the center of the frequency range (~81 MHz) to maximize the effect of inpainting on the power spectrum statistics. From top to bottom: delay power spectra (solid line) and error estimates (dotted line); ratio between the power spectrum error estimates derived from the full inpainting covariance vs. those derived from the conservative approximation described in Section 4.3; window functions around different delay bins.

Figure 11. Same as Figure 10, but with artificially flagged channels across all 14 nights in the observed HERA Phase II data.

underestimate the error. This is because even though the approximation agrees well with the diagonal terms in the full-covariance matrix, the off-diagonal terms make the error in the full-covariance approach higher. The two approaches do agree well at high delays and the differences at low delays are within 50% for flags that are narrower than 15-channel wide. On the other hand, when all 14 nights are flagged, our approximation actually overestimates the noise level. This is because as $N_{\rm sample}$ goes to zero, the estimated variance in the conservative approximation becomes extremely large.[34] This can be seen from our approximation for some of the channels near ~60 MHz in Figure 9. In the full-covariance matrix, these completely flagged channels do not have infinite uncertainties due to the sufficient amount of information from neighboring channels where we infer the best-fit inpainting model.

The bottom three panels of Figures 10 and 11 show the window functions with the effect of inpainting over these artificial flags. We see that in the case where the flagged channel only appears on one of the nights, the effect of inpainting on the window function is negligible, especially at high delays. When all 14 nights are flagged, however, we see that a flag that spans more than five channels can introduce significant correlation in the Fourier space even at high delays, making it crucial to correctly propagate the effect of inpainting into power spectrum statistics.

6. Conclusion

Power spectrum analyses in 21 cm cosmology are particularly sensitive to missing data or small discontinuities in the data along the frequency axis. These spectral structures can lead to the ringing of bright foreground modes in the Fourier space, contaminating a large area of modes that are, in theory, free of foreground signals.

In this work, we have identified a new source of discontinuities. This arises from averaging measurements that contain varying systematic effects and flagging patterns. Using a realistic simulation, we have shown (Figure 2) that time-varying flagging patterns can couple bright foreground modes with systematic effects in the Fourier space, making systematic effects that are otherwise below the noise level prominent in the 21 cm power spectrum. This effect can be seen even when each

---

[34] Formally speaking, the estimated variance goes to infinity as $N_{\rm sample}$ goes to zero. To regularize this behavior, we use the minimal nonzero value of $N_{\rm sample}$ across the frequency range where we inpaint instead of zero to estimate the noise variance at the channels that are completely flagged.

frequency channel in the averaged visibility contains more than 80% of unflagged data (Figure 3).

We have demonstrated that this discontinuity can be suppressed by inpainting data prior to averaging. However, as we inpaint over more and more data, it is crucial to correctly estimate the uncertainties associated with these methods. In this work, we have chosen to focus on inpainting via the the discrete prolate spheroidal sequence (DPSS; D. Slepian 1978; A. Ewall-Wice et al. 2021). Thanks to the linear nature of our inpainting method, we have developed a framework to incorporate the inpainting operation into the power spectrum quadratic estimator. This allows us to accurately quantify the effect of data inpainting on important statistical quantities such as the power spectrum error bar and window function (Figure 6).

We have applied the statistical tools developed in this work to inspect a small set of data obtained by the HERA Phase II instrument. To increase computational feasibility in future analyses, we have proposed and tested methods that can well approximate the power spectrum statistics. By artificially introducing flags into the real data, we have quantified the regime where we can safely adopt our proposed approximation and neglect the effect of inpainting (Figures 10 and 11). Our results provide a framework that allows us to carefully study gappy data in the ever more noisy RFI environment as we move toward detecting the 21 cm power spectrum.

This paper makes use of publicly accessible software developed for the HERA Collaboration[35] and software built by both HERA members and collaborators,[36] especially `pyuvdata` (B. J. Hazelton et al. 2017). Numerical calculations are performed through the Python packages `numpy` (C. R. Harris 2020) and `scipy` (P. Virtanen et al. 2020).

---

[35] https://github.com/Hera-Team
[36] https://github.com/RadioAstronomySoftwareGroup

Many of the cosmological and astrophysical calculations in this work rely on the routines wrapped up in `colossus` (B. Diemer 2018) and `astropy` (Astropy Collaboration et al. 2022). Plots are made available thanks to `matplotlib` (J. D. Hunter 2007) and `seaborn` (M. L. Waskom 2021).

Appendix
Probability Distribution Function of the Inpainted Visibility

In this appendix, we calculate the uncertainties in the inpainted visibility $v'_{\rm inp}$ in the flagged channels. Namely, we wish to know the probability of the unobserved $v'_{\rm inp}$ in the flagged channels given the observed visibility $v_{\rm obs}$, the noise covariance N, and the design matrix A that prescribes the shape of the underlying signal. Following Section 4.2, we have

$$P(v'|v_{\rm obs}, N, A) = \int db\, P(v'|b, N', A)P(b|v_{\rm obs}, N_{\rm u}, A), \quad (A1)$$

where

$$P(v'|b, N', A) \propto \exp[-(v'_{\rm inp} - P_{\rm f}Ab)^\dagger N'^{-1}_{\rm f}(v'_{\rm inp} - P_{\rm f}Ab)], \quad (A2)$$

and

$$P(b|v_{\rm obs}, N_{\rm u}, A) \propto P(v_{\rm obs}|b, N_{\rm u}, A)P(b) \propto \exp[-(v_{\rm obs} - Ab)^\dagger N_{\rm u}^{-1}(v_{\rm obs} - Ab)], \quad (A3)$$

assuming a flat prior on b. By taking $\partial P(b|v_{\rm obs}, N_{\rm u}, A)/\partial b = 0$, we can solve for the mean of the Gaussian distribution $P(b|v_{\rm obs}, N_{\rm u}, A)$ to be at[37]

$$\hat{b} = (A^\dagger N_{\rm u}^{-1}A)^{-1}A^\dagger N_{\rm u}^{-1}v_{\rm obs}. \quad (A4)$$

Meanwhile, by examining quadratic terms in the exponent, we know that the covariance must be $(A^\dagger N_{\rm u}^{-1}A)^{-1}$. Therefore, we can write

$$P(b|v_{\rm obs}, N_{\rm u}, A) \propto \exp[-(b - \hat{b})^\dagger (A^\dagger N_{\rm u}^{-1}A)(b - \hat{b})]. \quad (A5)$$

The integration in Equation (A1) can then be computed by "completing the square". We first note that we can rewrite $(v'_{\rm inp} - P_fAb)^\dagger N'^{-1}_{\rm f}(v'_{\rm inp} - P_fAb)$ into

$$\begin{aligned}
&(v'_{\rm inp} - P_{\rm f}Ab)^\dagger N'^{-1}_{\rm f}(v'_{\rm inp} - P_{\rm f}Ab) \\
&= v'^\dagger_{\rm inp}N'^{-1}_{\rm f}v'_{\rm inp} + b^\dagger A^\dagger P_{\rm f}^\dagger N'^{-1}_{\rm f}P_{\rm f}Ab + v'^\dagger_{\rm inp}N'^{-1}_{\rm f}P_{\rm f}Ab + b^\dagger A^\dagger P_{\rm f}^\dagger N'^{-1}_{\rm f}v'_{\rm inp} \\
&= v'^\dagger_{\rm inp}N'^{-1}_{\rm f}v'_{\rm inp} + b^\dagger(A^\dagger P_{\rm f}^\dagger N'^{-1}_{\rm f}P_{\rm f}A)b + \\
&\quad + b'^\dagger(A^\dagger P_{\rm f}^\dagger N'^{-1}_{\rm f}P_{\rm f}A)b + b^\dagger(A^\dagger P_{\rm f}^\dagger N'^{-1}_{\rm f}P_{\rm f}A)b' \\
&= (b - b')^\dagger(A^\dagger P_{\rm f}^\dagger N'^{-1}_{\rm f}P_{\rm f}A)(b - b') + v'^\dagger_{\rm inp}N'^{-1}_{\rm f}v'_{\rm inp} - b'^\dagger(A^\dagger P_{\rm f}^\dagger N'^{-1}_{\rm f}P_{\rm f}A)b',
\end{aligned} \quad (A6)$$

---

[37] Formally speaking, the matrix $A^\dagger N_{\rm u}^{-1}A$ might not be invertible as $N_{\rm u}$ is not full rank. However, $A^\dagger$ is a coordinate transformation that maps from a space of dimension $N_{\rm freq}$ to the space of DPSS coefficients. Since we have fewer DPSS modes than the number of frequency channels, here we will assume $A^\dagger N_{\rm u}^{-1}A$ is invertible. This assumption holds if we only have a small amount of channels that are flagged.

where we have defined $\mathbf{b}' \equiv (A^\dagger P_f^\dagger N_f'^{-1} P_f A)^{-1} A^\dagger P_f^\dagger N_f'^{-1} v'_{\text{inp}}$. Equation (A1) thus becomes

$$
\begin{aligned}
P(v'_{\text{inp}}|v_{\text{obs}}, N, A) &\propto \exp\left[-v'^{\dagger}_{\text{inp}} N_f'^{-1} v'_{\text{inp}} + \mathbf{b}'^{\dagger}(A^\dagger P_f^\dagger N_f'^{-1} P_f A)\mathbf{b}'\right] \\
&\times \int d\mathbf{b} \exp\left[-(\mathbf{b}-\mathbf{b}')^\dagger(A^\dagger P_f^\dagger N_f'^{-1} P_f A)(\mathbf{b}-\mathbf{b}') - (\mathbf{b}-\hat{\mathbf{b}})^\dagger(A^\dagger N_u^{-1} A)\right. \\
&\times (\mathbf{b}-\hat{\mathbf{b}})] \propto \exp\left[-v'^{\dagger}_{\text{inp}} N_f'^{-1} v'_{\text{inp}} + \mathbf{b}'^{\dagger}(A^\dagger P_f^\dagger N_f'^{-1} P_f A)\mathbf{b}'\right. \\
&\left. -(\mathbf{b}'-\hat{\mathbf{b}})^\dagger((A^\dagger N_u^{-1} A)^{-1} + (A^\dagger P_f N_f'^{-1} P_f A)^{-1})^{-1}(\mathbf{b}'-\hat{\mathbf{b}})\right]
\end{aligned}
$$
(A7)

To simplify the notation, we denote $C_u \equiv (A^\dagger N_u^{-1} A)^{-1}$ and $C_f \equiv (A^\dagger P_f^\dagger N_f'^{-1} P_f A)^{-1}$. Next, we will reduce Equation (A7) by "completing the square" again. First, we collect all the terms that are quadratic in v'_{inp}, noting that $\mathbf{b}' \equiv C_f A^\dagger P_f^\dagger N_f'^{-1} v'_{\text{inp}}$,

$$
\begin{aligned}
&-v'^{\dagger}_{\text{inp}} N_f'^{-1} v'_{\text{inp}} + \mathbf{b}'^{\dagger} C_f^{-1} \mathbf{b}' - \mathbf{b}'^{\dagger}(C_f + C_u)^{-1}\mathbf{b}' \\
&= -v'^{\dagger}_{\text{inp}}(N_f'^{-1} - (N_f'^{-1} A P_f C_f)(C_f^{-1} - (C_f + C_u)^{-1})(C_f A^\dagger P_f^\dagger N_f'^{-1}))v'_{\text{inp}}.
\end{aligned}
$$
(A8)

We now show that

$$
\begin{aligned}
C^{-1} &\equiv (N_f'^{-1} - (N_f'^{-1} P_f A C_f)(C_f^{-1} - (C_f + C_u)^{-1})(C_f A^\dagger P_f^\dagger N_f'^{-1}) \\
&= (N_f' + \mathcal{O}_{\text{inp}} N_u \mathcal{O}_{\text{inp}}^\dagger)^{-1},
\end{aligned}
$$
(A9)

where $\mathcal{O}'_{\text{inp}}$ is our proposed inpainting operator that maps observed data v_{obs} into a model that we use to inpaint the flagged channels,

$$
\mathcal{O}_{\text{inp}} \equiv P_f A (A^\dagger N_u^{-1} A)^{-1} A^\dagger N_u^{-1}.
$$
(A10)

To show this relation, we note that by the Woodbury matrix identity,

$$
(C_f + C_u)^{-1} = C_f^{-1} - C_f^{-1}(C_f^{-1} + C_u^{-1})C_f^{-1}.
$$
(A11)

Thus,

$$
(C_f^{-1} - (C_f + C_u)^{-1}) = C_f^{-1}(C_f^{-1} + C_u^{-1})C_f^{-1}.
$$
(A12)

This gives us

$$
(N_f'^{-1} A P_f C_f)(C_f^{-1} - (C_f + C_u)^{-1})(C_f A^\dagger P_f^\dagger N_f'^{-1}) = N_f'^{-1} A P_f(C_f^{-1} + C_u^{-1})A^\dagger P_f^\dagger N_f'.
$$
(A13)

Hence

$$
C^{-1} = N_f'^{-1} - N_f'^{-1} P_f A(C_f^{-1} + C_u^{-1})A^\dagger P_f^\dagger N_f'^{-1}.
$$
(A14)

On the other hand, the Woodbury matrix identity also gives us

$$
\begin{aligned}
(N_f' + \mathcal{O}_{\text{inp}} N_u \mathcal{O}_{\text{inp}}^\dagger)^{-1} &= (N_f' + P_f A (A^\dagger N_u^{-1} A)^{-1} A^\dagger P_f^\dagger)^{-1} \\
&= N_f'^{-1} - N_f'^{-1} P_f A(C_u^{-1} + A^\dagger P_f^\dagger N_f'^{-1} P_f A)A^\dagger P_f^\dagger N_f'^{-1} \\
&= N_f'^{-1} - N_f'^{-1} P_f A(C_u^{-1} + C_f^{-1})A^\dagger P_f^\dagger N_f'^{-1},
\end{aligned}
$$
(A15)

which agrees with Equation (A14). Thus we have shown that

$$
C = N_f' + \mathcal{O}_{\text{inp}} N_u \mathcal{O}_{\text{inp}}^\dagger.
$$
(A16)

To examine the rest of the terms in Equation (A7), we note that the term linear in v'_{inp} can be written as
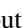
$$
\begin{aligned}
&\mathbf{b}'^{\dagger}(C_f + C_u)\hat{\mathbf{b}} \\
&= v'^{\dagger}_{\text{inp}} N_f'^{-1} P_f A C_f(C_f + C_u)\hat{\mathbf{b}} \\
&= v'^{\dagger}_{\text{inp}} N_f'^{-1} P_f A C_f(C_f^{-1} - C_f^{-1}(C_f^{-1} + C_u^{-1})C_f^{-1})\hat{\mathbf{b}} \\
&= v'^{\dagger}_{\text{inp}}(N_f'^{-1} P_f A - N_f'^{-1} P_f A(C_f^{-1} + C_u^{-1})A^\dagger P_f^\dagger N_f'^{-1} P_f A)\hat{\mathbf{b}} \\
&= v'^{\dagger}_{\text{inp}}(N_f'^{-1} - N_f'^{-1} P_f A(C_f^{-1} + C_u^{-1})A^\dagger P_f^\dagger N_f'^{-1})P_f A\hat{\mathbf{b}} \\
&= v'^{\dagger}_{\text{inp}} C^{-1} P_f A\hat{\mathbf{b}}.
\end{aligned}
$$
(A17)

Combining all these results, we finally arrive at

$$
P(v'_{\text{inp}}|v_{\text{obs}}, N, A) \propto \exp\left[-(v' - P_f A\hat{\mathbf{b}})^\dagger C^{-1}(v' - P_f A\hat{\mathbf{b}})\right],
$$
(A18)

where $C = N_f' + \mathcal{O}'_{\text{inp}} N_u \mathcal{O}'^{\dagger}_{\text{inp}}$, as promised in Equation (32). We note that while the derivation is quite complicated here, since everything is Gaussian in Equation (A1), it should not be surprising that we have arrived at a Gaussian distribution after performing this integration.

ORCID iDs

Kai-Feng Chen ⓘ https://orcid.org/0000-0002-3839-0230
Michael J. Wilensky ⓘ https://orcid.org/0000-0001-7716-9312
Adrian Liu ⓘ https://orcid.org/0000-0001-6876-0928
Joshua S. Dillon ⓘ https://orcid.org/0000-0003-3336-9958
Jacqueline N. Hewitt ⓘ https://orcid.org/0000-0002-4117-570X
James E. Aguirre ⓘ https://orcid.org/0000-0002-4810-666X
Adam P. Beardsley ⓘ https://orcid.org/0000-0001-9428-8233
Lindsay M. Berkhout ⓘ https://orcid.org/0000-0002-2293-9639
Gianni Bernardi ⓘ https://orcid.org/0000-0002-0916-7443
Judd D. Bowman ⓘ https://orcid.org/0000-0002-8475-2036

Philip Bull ⓘ https://orcid.org/0000-0001-5668-3101
Jacob Burba ⓘ https://orcid.org/0000-0002-8465-9341
Tyler Cox ⓘ https://orcid.org/0009-0008-2574-3878
David. R. DeBoer ⓘ https://orcid.org/0000-0003-3197-2294
Aaron Ewall-Wice ⓘ https://orcid.org/0000-0002-0086-7363
Steven R. Furlanetto ⓘ https://orcid.org/0000-0002-0658-1243
Adélie Gorce ⓘ https://orcid.org/0000-0002-1712-737X
Deepthi Gorthi ⓘ https://orcid.org/0000-0002-0829-167X
Bryna J. Hazelton ⓘ https://orcid.org/0000-0001-7532-645X
Daniel C. Jacobs ⓘ https://orcid.org/0000-0002-0917-2269
Nicholas S. Kern ⓘ https://orcid.org/0000-0002-8211-1892
Joshua Kerrigan ⓘ https://orcid.org/0000-0002-1876-272X
Piyanat Kittiwisit ⓘ https://orcid.org/0000-0003-0953-313X
Matthew Kolopanis ⓘ https://orcid.org/0000-0002-2950-2974
Paul La Plante ⓘ https://orcid.org/0000-0002-4693-0102

Yin-Zhe Ma ⓘ https://orcid.org/0000-0001-8108-0986
Andrei Mesinger ⓘ https://orcid.org/0000-0003-3374-1772
Miguel F. Morales ⓘ https://orcid.org/0000-0001-7694-4030
Steven G. Murray ⓘ https://orcid.org/0000-0003-3059-3823
Aaron R. Parsons ⓘ https://orcid.org/0000-0002-5400-8097
Robert Pascua ⓘ https://orcid.org/0000-0003-0073-5528
Yuxiang Qin ⓘ https://orcid.org/0000-0002-4314-1810
Mario G. Santos ⓘ https://orcid.org/0000-0003-3892-3073
Peter Sims ⓘ https://orcid.org/0000-0002-2871-0413
Jianrong Tan ⓘ https://orcid.org/0000-0001-6161-7037

References

Abdurashidova, Z., Aguirre, J. E., Alexander, P., et al. 2022, ApJ, 925, 221
Abrial, P., Moudden, Y., Starck, J. L., et al. 2008, StMet, 5, 289
Amiri, M., Bandura, K., Chen, T., et al. 2023, ApJ, 947, 16
Ansah-Narh, T., Abdalla, F. B., Smirnov, O. M., Asad, K. M. B., & Shaw, J. R. 2018, MNRAS, 481, 2694
Armel Mbou Sob, U., Landman Bester, H., Smirnov, O., Kenyon, J., & Grobler, T. 2019, arXiv:1910.08136
Astropy Collaboration, Price-Whelan, A. M., Lim, P. L., et al. 2022, ApJ, 935, 167
Barry, N., Hazelton, B., Sullivan, I., Morales, M. F., & Pober, J. C. 2016, MNRAS, 461, 3135
Barry, N., Wilensky, M., Trott, C. M., et al. 2019, ApJ, 884, 1
Beardsley, A. P., Hazelton, B. J., Sullivan, I. S., et al. 2016, ApJ, 833, 102
Berkhout, L. M., Jacobs, D. C., Abdurashidova, Z., et al. 2024, PASP, 136, 045002
Bharadwaj, S., Pal, S., Choudhuri, S., & Dutta, P. 2019, MNRAS, 483, 5694
Bowman, J., & Rogers, A. E. E. 2010, in RFI Mitigation Workshop (Trieste: PoS), 30
Bull, P., Ferreira, P. G., Patel, P., & Santos, M. G. 2015, ApJ, 803, 21
Burba, J., Bull, P., Wilensky, M. J., et al. 2024, MNRAS, 535, 793
Byrne, R. 2023, ApJ, 943, 117
Byrne, R., Morales, M. F., Hazelton, B., et al. 2019, ApJ, 875, 70
Chakraborty, A., Datta, A., & Mazumder, A. 2022, ApJ, 929, 104
Chakraborty, A., Datta, A., Roy, N., et al. 2021, ApJL, 907, L7
Chang, T.-C., Pen, U.-L., Peterson, J. B., & McDonald, P. 2008, PhRvL, 100, 091303
CHIME Collaboration, Amiri, M., Bandura, K., et al. 2022, ApJS, 261, 29
CHIME Collaboration, Amiri, M., Bandura, K., et al. 2024, ApJ, 963, 23
Choudhuri, S., Bull, P., & Garsden, H. 2021, MNRAS, 506, 2066
Cox, T. A., Parsons, A. R., Dillon, J.S., Ewall-Wice, A., & Pascua, R. 2024, MNRAS, 532, 3375
Crichton, D., Aich, M., Amara, A., et al. 2022, JATIS, 8 1 011019
Datta, A., Bowman, J. D., & Carilli, C. L. 2010, ApJ, 724, 526
de Oliveira-Costa, A., & Tegmark, M. 2006, PhRvD, 74, 023005
de Oliveira-Costa, A., Tegmark, M., Gaensler, B.M., et al. 2008, MNRAS, 388, 247
DeBoer, D. R., Parsons, A. R., Aguirre, J. E., et al. 2017, PASP, 129, 045001
Di Vruno, F., Winkel, B., Bassa, C. G., et al. 2023, A&A, 676, A75
Diemer, B. 2018, ApJS, 239, 35
Dillon, J., & Murray, S. 2023, H6C Internal Data Release 2.2 HERA Memo #125, https://reionization.org/manual_uploads/HERA125_H6C_IDR_2_2_Memo.pdf
Dillon, J., Murray, S., Cox, T.A., & Martinot, Z. E. 2024, H6C Internal Data Release 2.3 HERA Memo #131, https://reionization.org/manual_uploads/HERA131_H6C_IDR_2_3_Memo.pdf
Dillon, J. S., Liu, A., Williams, C. L., et al. 2014, PhRvD, 89, 023002
Dillon, J. S., Lee, M., Ali, Z. S., et al. 2020, MNRAS, 499, 5840
Dillon, J. S., Neben, A. R., Hewitt, J. N., et al. 2015, PhRvD, 91, 123011
Eastwood, M. W., Anderson, M. M., Monroe, R. M., et al. 2019, AJ, 158, 84
Elahi, K. M. A., Bharadwaj, S., Chatterjee, S., et al. 2024, arXiv:2410.11380
Ewall-Wice, A., Dillon, J. S., Hewitt, J. N., et al. 2016, MNRAS, 460, 4320
Ewall-Wice, A., Dillon, J. S., Liu, A., & Hewitt, J. 2017, MNRAS, 470, 1849
Ewall-Wice, A., Kern, N., Dillon, J. S., et al. 2021, MNRAS, 500, 5195
Feeney, S. M., Peiris, H. V., & Pontzen, A. 2011, PhRvD, 84, 103002
Furlanetto, S. R., Oh, S. P., & Briggs, F. H. 2006, PhR, 433, 181
Garsden, H., Bull, P., Wilensky, M., et al. 2024, MNRAS, 535, 3218
Garsden, H., Greenhill, L., Bernardi, G., et al. 2021, MNRAS, 506, 5802
Gehlot, B. K., Mertens, F. G., Koopmans, L. V. E., et al. 2019, MNRAS, 488, 4271
Ghosh, A., Bharadwaj, S., Ali, S. S., & Chengalur, J. N. 2011, MNRAS, 411, 2426
Gorce, A., Ganjam, S., Liu, A., et al. 2023, MNRAS, 520, 375
Grigg, D., Tingay, S. J., Sokolowski, M., et al. 2023, A&A, 678, L6
Gruetjen, H. F., Fergusson, J. R., Liguori, M., & Shellard, E. P. S. 2017, PhRvD, 95, 043532
Gupta, Y., Ajithkumar, B., Kale, H. S., et al. 2017, CSci, 113, 707
Harris, F. J. 1978, IEEEP, 66, 51
Harris, C. R., Millman, K. J., van der Walt, S. J., et al. 2020, Natur, 585, 357
Hazelton, B. J., Jacobs, D. C., Pober, J. C., & Beardsley, A. P. 2017, JOSS, 2, 140
Hazelton, B. J., Morales, M. F., & Sullivan, I. S. 2013, ApJ, 770, 156
HERA Collaboration, Abdurashidova, Z., Adams, T., et al. 2023, ApJ, 945, 124
Högbom, J. A. 1974, A&AS, 15, 417
Hunter, J. D. 2007, CSE, 9, 90
Hurley-Walker, N., Callingham, J. R., Hancock, P. J., et al. 2017, MNRAS, 464, 1146
Hurley-Walker, N., Hancock, P. J., Franzen, T. M. O., et al. 2019, PASA, 36, e047
Josaitis, A. T., Ewall-Wice, A., Fagnoni, N., & de Lera Acedo, E. 2022, MNRAS, 514, 1804
Joseph, R. C., Trott, C. M., & Wayth, R. B. 2018, AJ, 156, 285
Joseph, R. C., Trott, C. M., Wayth, R. B., & Nasirudin, A. 2020, MNRAS, 492, 2017
Karnik, S., Romberg, J., & Davenport, M.A. 2020, arXiv:2006.00427
Kennedy, F., Bull, P., Wilensky, M. J., Burba, J., & Choudhuri, S. 2023, ApJS, 266, 23
Kern, N. S., & Liu, A. 2021, MNRAS, 501, 1463
Kern, N. S., Parsons, A. R., Dillon, J. S., et al. 2019, ApJ, 884, 105
Kim, H., Nhan, B. D., Hewitt, J. N., et al. 2022, ApJ, 941, 207
Kolopanis, M., Jacobs, D. C., Cheng, C., et al. 2019, ApJ, 883, 133
Koopmans, L., Pritchard, J., Mellema, G., et al. 2015, in Advancing Astrophysics with the Square Kilometre Array (AASKA14) (Trieste: PoS), 1
Li, W., Pober, J. C., Barry, N., et al. 2019, ApJ, 887, 141
Li, W., Pober, J. C., Hazelton, B. J., et al. 2018, ApJ, 863, 170
Liu, A., Parsons, A. R., & Trott, C. M. 2014, PhRvD, 90, 023018
Liu, A., & Shaw, J. R. 2020, PASP, 132, 062001
Liu, A., & Tegmark, M. 2011, PhRvD, 83, 103006
Liu, A., Tegmark, M., Morrison, S., Lutomirski, A., & Zaldarriaga, M. 2010, MNRAS, 408, 1029
Lomb, N. R. 1976, Ap&SS, 39, 447
Lourenço, L., Chippendale, A. P., Indermuehle, B., et al. 2024, PASA, 41, e012
Mertens, F. G., Ghosh, A., & Koopmans, L. V. E. 2018, MNRAS, 478, 3640
Mertens, F. G., Mevius, M., Koopmans, L. V. E., et al. 2020, MNRAS, 493, 1662
Mesinger, A. 2016, in Understanding the Epoch of Cosmic Reionization: Challenges and Progress (Berlin: Springer)
Mitchell, D.A., Greenhill, L. J., Wayth, R. B., et al. 2009, RaSc, 44, 0A01
Morales, M. F., Hazelton, B., Sullivan, I., & Beardsley, A. 2012, ApJ, 752, 137
Morales, M. F., & Wyithe, J. S. B. 2010, ARA&A, 48, 127
Mouri Sardarabadi, A., & Koopmans, L. V. E. 2019, MNRAS, 483, 5480
Munshi, S., Mertens, F. G., Koopmans, L. V. E., et al. 2024, A&A, 681, A62
Murray, S., Dillon, J., & Martinot, Z.E. 2023, H6C Internal Data Release 2.1 HERA Memo #124, https://reionization.org/manual_uploads/HERA124_H6C_IDR_2_Memo_v3.pdf
Neben, A. R., Bradley, R. F., Hewitt, J. N., et al. 2016b, ApJ, 826, 199
Neben, A. R., Hewitt, J. N., Bradley, R. F., et al. 2016a, ApJ, 820, 44
Offringa, A. R., de Bruyn, A. G., Zaroubi, S., et al. 2013, A&A, 549, A11
Offringa, A. R., Mertens, F., & Koopmans, L. V. E. 2019, MNRAS, 484, 2866
Offringa, A. R., van de Gronde, J.J., & Roerdink, J.B.T.M. 2012, A&A, 539, A95
Offringa, A. R., Wayth, R. B., Hurley-Walker, N., et al. 2015, PASA, 32, e008
Orosz, N., Dillon, J. S., Ewall-Wice, A., Parsons, A. R., & Thyagarajan, N. 2019, MNRAS, 487, 537
Paciga, G., Albert, J. G., Bandura, K., et al. 2013, MNRAS, 433, 639
Pagano, M., Liu, J., Liu, A., et al. 2023, MNRAS, 520, 5552
Pal, S., Bharadwaj, S., Ghosh, A., & Choudhuri, S. 2021, MNRAS, 501, 3378
Parsons, A. R., & Backer, D. C. 2009, AJ, 138, 219
Parsons, A. R., Backer, D. C., Foster, G. S., et al. 2010, AJ, 139, 1468
Parsons, A. R., Liu, A., Aguirre, J. E., et al. 2014, ApJ, 788, 106
Parsons, A. R., Pober, J. C., Aguirre, J. E., et al. 2012, ApJ, 756, 165
Pascua, R., Martinot, Z. E., Liu, A., et al. 2024, arXiv:2410.01872
Patil, A., Yatawatta, S., Koopmans, L., et al. 2017, ApJ, 838, 65
Patil, A. H., Yatawatta, S., Zaroubi, S., et al. 2016, MNRAS, 463, 4317
Paul, S., Santos, M. G., Chen, Z., & Wolz, L. 2023, arXiv:2301.11943

Pritchard, J. R., & Loeb, A. 2012, RPPh, 75, 086901
Rath, E., Dynes, S., Hewitt, J., & Molewa, M. 2021, Motion of HERA Antenna Feeds, https://api.semanticscholar.org/CorpusID:232128217
Rath, E., Pascua, R., Josaitis, A. T., et al. 2024, arXiv:2406.08549
Roberts, D. H., Lehar, J., & Dreher, J. W. 1987, AJ, 93, 968
Rybicki, G. B., & Press, W. H. 1992, ApJ, 398, 169
Santos, M., Bull, P., Alonso, D., et al. 2015, in Advancing Astrophysics with the Square Kilometre Array (AASKA14) (Trieste: PoS), 19
Santos, M., Bull, P., Camera, S., et al. 2016, in MeerKAT Science: On the Pathway to the SKA (Trieste: PoS), 32
Scargle, J. D. 1982, ApJ, 263, 835
Sievers, J. L. 2017, arXiv:1701.01860
Sihlangu, I., Oozeer, N., & Bassett, B.A. 2020, arXiv:2008.08877
Sims, P. H., Pober, J. C., & Sievers, J. L. 2022, MNRAS, 517, 910
Slepian, D. 1978, ATTTJ, 57, 1371
Sokolowski, M., Wayth, R. B., & Lewis, M. 2016, arXiv:1610.04696
Starck, J. L., Fadili, M. J., & Rassat, A. 2013, A&A, 550, A15
Sullivan, I. S., Morales, M. F., Hazelton, B. J., et al. 2012, ApJ, 759, 17
Tan, J., Liu, A., Kern, N. S., et al. 2021, ApJS, 255, 26
Thyagarajan, N., Udaya Shankar, N., Subrahmanyan, R., et al. 2013, ApJ, 776, 6
Tingay, S. J., Goeke, R., Bowman, J. D., et al. 2013, PASA, 30, e007
Trott, C. M., Jordan, C. H., Midgley, S., et al. 2020, MNRAS, 493, 4711
Trott, C. M., Pindor, B., Procopio, P., et al. 2016, ApJ, 818, 139

Trott, C. M., Wayth, R. B., & Tingay, S. J. 2012, ApJ, 757, 101
Ung, D. C. X., Sokolowski, M., Sutinjo, A.T., & Davidson, D.B. 2020, ITAP, 68, 5395
van Haarlem, M. P., Wise, M. W., Gunst, A. W., et al. 2013, A&A, 556, A2
Vanderlinde, K., Liu, A., Gaensler, B., et al. 2019, Canadian Long Range Plan for Astronomy and Astrophysics White Papers, Zenodo, doi:10.5281/zenodo.3765414
Vaníček, P. 1969, Ap&SS, 4, 387
Vaníček, P. 1971, Ap&SS, 12, 10
Vedantham, H., Udaya Shankar, N., & Subrahmanyan, R. 2012, ApJ, 745, 176
Virtanen, P., Gommers, R., Oliphant, T. E., et al. 2020, NatMe, 17, 261
Waskom, M. L. 2021, JOSS, 6, 3021
Wayth, R. B., Tingay, S. J., Trott, C. M., et al. 2018, PASA, 35, e033
Wilensky, M. J., Hazelton, B. J., & Morales, M. F. 2022, MNRAS, 510, 5023
Wilensky, M. J., Morales, M. F., Hazelton, B. J., et al. 2019, PASP, 131, 114507
Wilensky, M. J., Morales, M. F., Hazelton, B. J., et al. 2023, ApJ, 957, 78
Yatawatta, S., Zaroubi, S., de Bruyn, G., Koopmans, L., & Noordam, J. 2008, arXiv:0810.5751
Yoshiura, S., Pindor, B., Line, J. L. B., et al. 2021, MNRAS, 505, 4775
Zarka, P., Girard, J. N., Tagger, M., & Denis, L. 2012, in SF2A-2012: Proc. Annual Meeting of the French Society of Astronomy and Astrophysics, ed. S. Boissier et al. (Paris: SF2A), 687
Zheng, H., Tegmark, M., Dillon, J. S., et al. 2017, MNRAS, 464, 3486